Institut für Geowissenschaften
Friedrich-Schiller-Universität Jena

Max Planck Institute
for Biogeochemistry

# MASTER THESIS

**MAX PLANCK INSTITUTE FOR BIOGEOCHEMISTRY, JENA**
**INSTITUTE OF GEOSCIENCE, FRIEDRICH-SCHILLER-UNIVERSITY JENA**

## MINERAL-ASSOCIATED CARBON IN MANGROVE ECOSYSTEMS IN THE SINÚ RIVER DELTA, COLOMBIA


**BY:** HEIDI VÖLKEL
**MATRICULATION NUMBER:** 118921
**E-MAIL:** heidi.voelkel@uni-jena.de

**SUPERVISOR FSU JENA:** PROF. DR. JURAJ MAJZLAN
**SUPERVISOR MPI-BGC JENA:** DR. CARLOS A. SIERRA


**DEADLINE:** JANUARY 05, 2017

**Abstract**

The objective of this master thesis is to clarify the question: Where do unusually high carbon contents in the mangrove area of Cispatá bay in Colombia have their origin? To answer this question, carbon contents of 75 collected samples had to be determined first. Further, a mineralogical analysis was conducted, as well as the determination of isotopic signatures ($\delta^{13}$C, $\Delta^{14}$C), and concentrations of aluminum- and iron oxides. The results of those measurements were statistically evaluated and represented graphically. Differences in carbon stocks were found especially between basin and fringe mangroves, whereby basin soils show much higher total organic carbon concentrations. Moreover, basin soils are not only much older than fringe soils, primarily in deeper layers, but they also show less plant derived $^{13}$C signatures and higher aluminum- and iron contents. They both have the same qualitative composition of the mineral fraction, but fringe soils contain a smaller mineral soil portion and a higher portion of organic carbon. I conclude that, first, carbon is produced in situ both in fringe and basin mangroves. $^{13}$C and $^{14}$C signatures show, that additionally entered carbon has a terrestrial origin, which enters the mangrove area via the Sinú river. It is bound to the mineral fraction, especially in basin forests, where the ground structure slows additionally the drainage of dissolved carbon into the ocean.

# Declaration Of Originality

I confirm that this assignment, entitled *'Mineral-associated carbon in mangrove ecosystems in the Sinú river delta, Colombia'*, is my own work and that I have not sought or used inadmissible help of third parties. I have clearly referenced all sources used in the work. This work has not yet been submitted to another examination institution, neither in Germany nor outside Germany, neither in the same nor in a similar way and has not yet been published. Hereby, I agree on the public inspection of my master thesis.

Jena, January 5, 2017

..... (signature)

# Acknowledgements

At this point I would like to take the opportunity to thank Prof. Dr. Juraj Majzlan for enabling the work on the topic of my interest, his outstanding support, engagement and critical hints. I would like to give special thanks to Dr. Carlos A. Sierra, who made it possible to work on this exciting topic at the Max-Planck-Institute for Biogeochemistry, his excellent support, suggestions and time exposure for showing me dealing with scientific software. Thanks also for the great time in Colombia together with Jhoanata Bolívar, who enabled me to participate at the soil sampling in Cispatá bay.

I would also like to thank Jörn Engelhardt for creating overview maps using ArcGis, Frank Linde for processing the clay mineral fraction of my samples at the Institute of Geosciences and Ralph Bolanz for his help during the preparation of XRD measurements and the interpretation of diffractograms. Thanks to Ines Hilke, Iris Kuhlmann and Heike Geilmann for their help during the preparation of analytical measurements at the Max-Planck-Institute as well as to Holger Metzler, Markus Müller and Verónica Ceballos-Núñez, who were always open for questions.

Thanks also to the financial support for the development of this thesis project, which was provided by the Alexander von Humboldt Foundation and the Max-Planck-Institute for Biogeochemistry.

Special thanks go also to my dear family and friends, without whom, completing my master programme would be impossible.

# Contents

# List Of Abbreviations

| | |
|---|---|
| **C** | Carbon |
| **DOM** | Dissolved Organic Matter |
| **IC** | Inorganic Carbon |
| **IGW** | Institute For Geosciences |
| **MPI-BGC** | Max-Planck-Institute for Biogeochemistry Jena |
| **N** | Nitrogen |
| **OC** | Organic Carbon |
| **OM** | Organic Matter |
| **TC** | Total Carbon |
| **TCD** | Thermal Conductivity Detector |
| **TN** | Total Nitrogen |
| **TOC** | Total Organic Carbon |
| **VPDB** | Vienna Pee Dee Belemnite |
| **XRD** | X-Ray Diffraction |

# List of Figures

# 1 Introduction

## 1.1 Motivation And Main Objective

Sediments in the mangrove forests of the Sinú river delta in Colombia show unusually large differences of carbon concentrations between basin- and fringe mangroves. A previous study (Bolívar et al., 2015) showed that for the basin mangroves, total organic carbon (TOC) is 740±40 MgC/ha, while for the fringe mangroves this value is only 95±9 MgC/ha. Compared to other mangrove ecosystems, especially the basin mangrove carbon content of the Sinú river delta is extremely high. An example for this is Gazi bay in Kenya, where the mangrove soil shows an average carbon content of only 36.55 MgC/ha at a sampling depth of 60 cm (Tamooh et al., 2008). Another example is Okinawa Island in Japan, where the TOC content is 57.30 MgC/ha at a sampling depth of 1 m (Khan et al., 2007).

It is unknown whether the high concentrations of carbon in Cispatá bay are terrestrially derived and transported by the river or whether they are produced in situ by the mangroves. Sediments in the delta region have entered on the one hand downriver across the Andes and on the other hand from marine tides over the Caribbean. Using analyses of mineralogy (Al- and Fe-oxides, clay minerals) as well as elemental and isotopic analyses of carbon, the origin of high carbon contents in these soils can be determined (Spohn and Giani, 2012; Spohn et al., 2013). It is important to ascertain, if the sediments of the mangroves have terrestrial or marine origin. Probably the changing of the course of the river is also crucial for the increased carbon levels in certain regions. The origin of high carbon contents needs to be examined using the analytical groundwork.

## 1.2 Specific Objectives

1. *To determine C and N concentrations in two types of mangroves*
   This information helps to determine, how much C and N is produced autochthonous by the local vegetation and soil organisms. Furthermore the results provide the concentration of mineral-bonded C, which is either terrestrially derived or marine entered via tidal flooding.

2. *To use the $\delta^{13}C$ and $\Delta^{14}C$ signatures of the carbon to explore its origin*
   According to Middelburg and Herman (2007), $\delta^{13}$C signatures have been shown to be very useful for differentiating sources of OM in coastal water and estuaries. The objective is therefore to find out the average $\delta^{13}$C signatures for basin and fringe mangroves and to correlate them with the isotopic signatures of the end-members (chapter 2.1). The same applies to $\Delta^{14}$C signatures, with the difference, that here ages can be compared.

3. *To determine Fe and Al oxides as proxies for mineral bound carbon*
   This is a third indicator for the carbon source in the mangrove area. Mineral surface complexation-ligand exchange reactions between OM and metal oxide surfaces are noted in many studies (Gu et al., 1995). Because those mineral surfaces adsorb OM, the terrestrial origin for additionally entered carbon can be determined indirectly.

4. *To use analyses of clay minerals to determine the potential origin of the sediments*
   It is necessary to determine the clay mineral composition in the soils, because OM can be adsorbed on clay mineral surfaces (e.g. illite and kaolinite surfaces (Gu et al., 1995)). It is assumed, that several samples contain a high proportion of clays, which can be one of the main suppliers for downriver entered mineral-bonded carbon.

Those specific objectives were defined to provide evidence for the following hypotheses:

1. Sediments in the mangrove forest of Cispatá bay show significant differences in carbon stocks between basin- and fringe mangroves

2. Additional entered carbon has its origin both in alluvial deposits through tidal flooding in Cispatá bay and in sedimentation via the Sinú river delta estuary

3. Transformed Al and Fe oxides and hydroxides build one main supplier for additional carbon

## 1.3 The Distribution Of Mangroves

The term mangrove implies all evergreen halophytic (salt-tolerant) species of tropical trees and shrubs with a population occurring in the tropics and subtropics between the latitudes of 30° north and south. The term mangrove includes, depending on classification, approximately 16 families and 40 to 50 species (Tomlinson, 1986). The global distribution of mangroves is delimited by major ocean currents and the 20°C isotherm of seawater in winter (Alongi, 2009). As shown in figure 1, there are two centres of mangrove diversity: The Eastern group (Indonesia, Australia, East Africa and the Western Pacific) where the total number of mangrove species is about 40; and the Western group (Caribbean, Florida and Atlantic South America) where the number of species is only ∼8 (Feller and Sitnik, 1996).

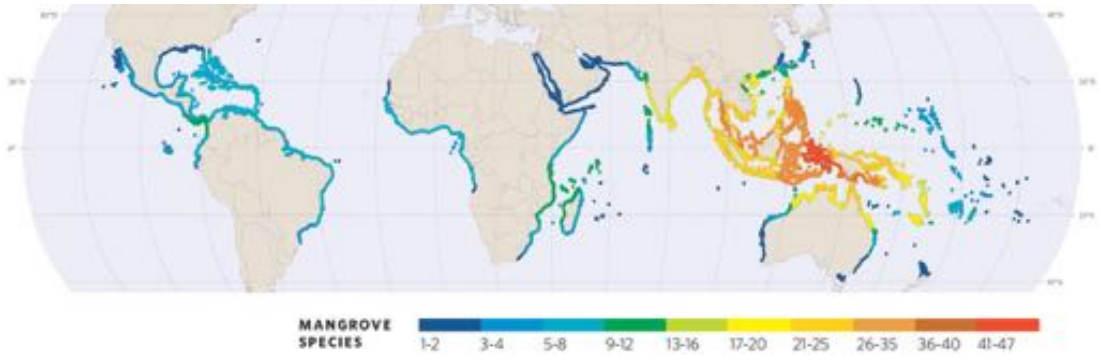


*Figure 1: World map of the mangrove distribution zones and the number of mangrove species along each region (National Oceanic and Atmospheric Administration, 2014)*

According to Giri et al. (2011) the largest extent of mangroves is found in Asia (42%) followed by Africa (20%), Central America (15%), Oceania (12%) and South America (11%). Approximately 75% of mangroves are concentrated in just 15 countries (compare table 1). Moreover, the largest percentage of mangroves is found between the latitudes of 5° north and south (figure 2).

*Table 1: The 15 most mangrove-rich countries and their cumulative percentage (Giri et al., 2011)*

| Number | Country | Area (ha) | % of global total | Cumulative % | Region |
|---|---|---|---|---|---|
| 1 | Indonesia | 3,112,989 | 22.6 | 22.6 | Asia |
| 2 | Australia | 977,975 | 7.1 | 29.7 | Oceania |
| 3 | Brazil | 962,683 | 7.0 | 36.7 | South America |
| 4 | Mexico | 741,917 | 5.4 | 42.1 | Central America |
| 5 | Nigeria | 653,669 | 4.7 | 46.8 | Africa |
| 6 | Malaysia | 505,386 | 3.7 | 50.5 | Asia |
| 7 | Myanmar (Burma) | 494,584 | 3.6 | 54.1 | Asia |
| 8 | Papua New Guinea | 480,121 | 3.5 | 57.6 | Oceania |
| 9 | Bangladesh | 436,570 | 3.2 | 60.8 | Asia |
| 10 | Cuba | 421,538 | 3.1 | 63.9 | Central America |
| 11 | India | 368,276 | 2.7 | 66.6 | Asia |
| 12 | Guinea Bissau | 338,652 | 2.5 | 69.1 | Africa |
| 13 | Mozambique | 318,851 | 2.3 | 71.4 | Africa |
| 14 | Madagascar | 278,078 | 2.0 | 73.4 | Africa |
| 15 | Philippines | 263,137 | 1.9 | 75.3 | Asia |

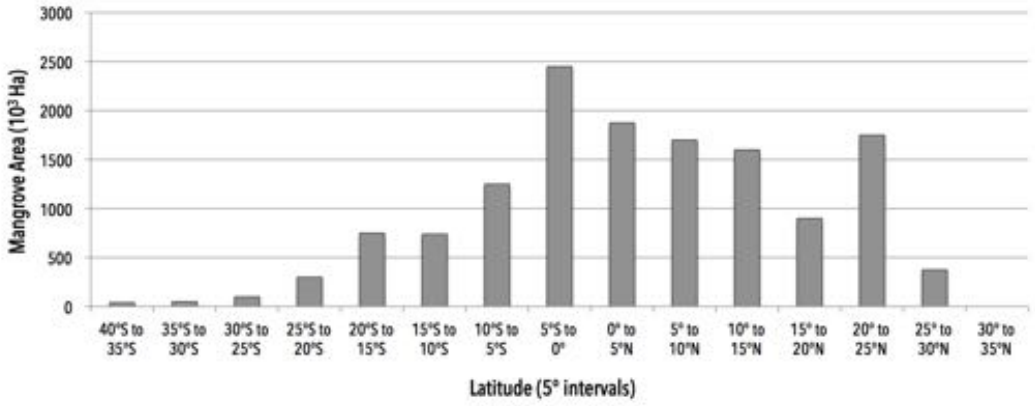


*Figure 2: Latitudinal distribution of mangrove forests on earth (Giri et al., 2011)*

In these distribution zones, mangroves occur at tidal- and transitional zones between marine and terrestrial environments. More detailed, they grow in river deltas, lagoons and estuarine complexes, as well as on shorelines and islands that are sheltered from wave action. Mangrove trees are adapted to harsh environmental settings such as (Giri et al., 2011):

- ◇ high salinity of the water
- ◇ high temperatures
- ◇ high tides (maximum amplitudes of 50 cm) and sedimentation rates
- ◇ anaerobic conditions and root zone anoxia
- ◇ high sulfide concentrations in the soil
- ◇ low light due to shading
- ◇ crab predation of seeds and propagules

## 1.4 Mangrove Ecosystems

As an adaption to the listed environmental conditions, mangroves develop a pronounced root system. Stilt roots or prop roots function as a foothold during tide- and tropical storms. Knee roots and pneumatophores grow vertically upwards

because oxygen can not be absorbed from the soil but only from air. Aerial roots grow down vertically on boughs to absorb nutrients and rainwater. As soon as the aerial roots anchor themselves in the ground, they obtain an additional holding function.


*Figure 3: Mangrove root types: Left - prop and aerial roots, middle - knee roots, right - pneumatophores*

According to Elmqvist and Cox (1996), mangroves have one of the most unique reproductive strategies in the plant world. Like most mammals, mangroves are viviparous, rather than producing dormant resting seeds like most flowering plants. Vivipary is the condition whereby the embryo (within the seed) grows first to break through the seed coat and then out of the fruit wall while it is still attached to the maternal parent. Mangroves disperse those propagules via water.

Considering the physical and morphological aspects of vegetation, mangroves are divided into different species using the parameters: roots, trunks and canopy. The most important species within the discussed study area of Cispatá bay are:

1. Red mangrove *(Rhizophora mangle)*

   *R. mangle* grows in deeper waters and develops large prop-roots, which provide the plant with stability towards tides, huge waves or tropical storms along the coastline. Prop and stilt-roots arise from the trunk of the mangrove and grow towards the soil where they develop an underground root system. Another important ability of stilt roots is to allow the exchange of oxygen in the oxygen-poor soil using lenticels, which enable the gas exchange. *R. mangle* prefers muddy, oxygen-poor soils along estuarine banks. These muddy soils are flooded daily by the tides and are mostly inhabited by numerous crustaceans which decompose biomass such as falling leaves and blossoms quickly. The thick and leathery evergreen leaves of *R. mangle* have a broadly-elliptical shape and are between 6 - 12 cm long and about 3 - 6 cm wide. *R. mangle* develops 3 - 5 cm brown fruits hosting the viviparous propagules. After separating itself from the fruit and the mother tree, propagules can survive in salt water for over a year, before they emerge primary roots and primary leaves in a favourable area. They can grow up to 40 cm in length, what distinguishes them from the other mangrove types. The designation 'red' comes from the tannins built in their roots under reductive and acidic conditions. In combination with ferric ions in the soil, surrounding water and mud turn into a rusty colour (Tomlinson, 1986).

2. Black mangrove *(Avicennia germinans)*

   *A. germinans* live further inland, protected from wave action and strong winds. They are less tolerant of highly saline conditions than certain other mangrove species. *A. germinans* only grow pneumatophores for gas exchanges, but no prop-roots. Black Mangroves have oblong to elliptical, evergreen leaves, 5 - 12 cm long and 2 - 4 cm wide, with smooth, slightly curled margins. The leaves are hairy below and often appear whitish from

the salt excreted at night and on cloudy days. The fruit is 3 - 5 cm long and the hosting viviparous propagules reach only a length of 3 cm. They can survive in salt water for at least 4 months. They are called 'black' mangroves, because the older sections of the trunk and heartwood are blackish in colour (Thibodeau and Nickerson, 1986).

3. White mangrove *(Laguncularia racemosa)*
   White mangroves live the farthest away from the water, just above the water level. They sometimes have pneumatophores, but they are usually less common. When pneumatophores are present they are shorter than those of black mangroves (knee-roots). The leaves are elliptical, 12 - 18 cm long and 2.5 - 5 cm wide and have two small glands at the base that exude sugars. The fruit is a reddish-brown drupe, about 12 - 20 mm long, with longitudinal ridges. The single seed is semi-viviparous (germination during dispersal). Viviparous propagules, which can grow up to 5 cm, can survive in salt water for at least 1 month. The name 'white' is given because of the whitish appearance of the bark (Tomlinson, 1986).

Mangroves often occur in zones, which are groupings of the same species of mangrove within a whole mangrove forest. Zonation occurs because different species of mangrove require particular conditions to grow. Some species require more water than others, or some species are able to tolerate more saline soils than others (Lewis et al., 2006). The zonation patterns may therefore differ on a local scale, depending on topographical landforms. The zonation patterns also differ on a global scale. The large variation in floristic composition of mangrove communities means that patterns of species distribution across the intertidal zone will vary substantially among geographic regions. For example, patterns for Florida and Caribbean mangroves often show *R. mangle* occupying the seaward zone, followed by *A. germinans* and *L. racemosa* in the most landward position. This pattern is

different in Australia or Indonesia, where the number of species is more then 20.

Different mangrove species often build huge communities of trees depending on environmental factors such as salinity. A distinction is made between 6 different mangrove forests. For Cispatá Bay two of them are important, known as fringe and basin forests (Lugo and Snedaker, 1974). Table 2 shows main representatives of each mangrove species of the respective forest type. While white mangroves are nearly intermediate in their occurrence, fringe forests are dominated by red mangroves and basin forests by black mangroves.

*Table 2: Contribution of every mangrove species to the Importance Value Index (Bolívar et al., 2015)*

| | Type of mangrove forest | |
|---|---|---|
| Species | Basin | Fringe |
| Rhizophora mangle | 68.16 | **218.58** |
| Laguncularia racemosa | 12.65 | 37.96 |
| Avicennia germinans | **219.20** | 43.45 |

Fringe mangrove forests grow along the fringes of protected shorelines and islands. They are influenced by tides and sea waves and also exposed to strong winds. This influence causes that fringe forests do not receive the amount of nutrients as mangroves in riverine forests and do not grow as high as other forest types.

Basin mangrove forests occur in inland areas along drainage depressions, which are flooded occasionally during the dry season and regularly during the wet season. They receive nutrients mainly by recycling vegetation debris. During dry season, the water level in the basin continues to decrease very slowly, caused by the groundwater flow discharging to the open sea. Therefore the salinity in the soil is high. In general, basin mangroves have a larger variability in vegetation

structure than fringe mangroves, depending on their distance to rivers and lagoons (Lugo and Snedaker, 1974). In the more coastal position, the basin forest of Cispatá Bay is dominated by *R. mangle*. Traversing inland this dominance becomes increasingly shared with the black mangrove *A. germinans* (Fig. 4).

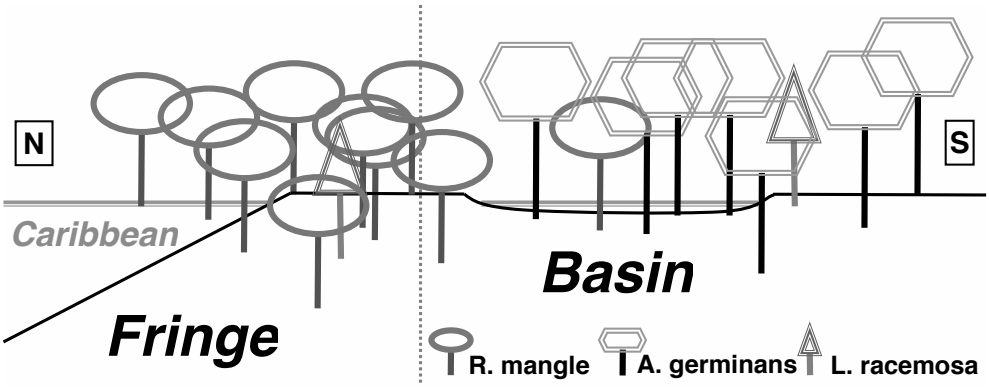


*Figure 4: Mangrove forest types of Cispatá bay*

## 1.5 Mangroves And Climate Change

Mangrove forests once covered more than 200.000 km$^2$ of sheltered tropical and subtropical coastlines. They are disappearing worldwide by 1 to 2 % per year, which is a greater rate than the decline of coral reefs or tropical rainforests (Duke et al., 2007). Owing to deforestation rates caused by large-scale conversion for fish and shrimp farming, tourism, pollution, and natural disasters, mangroves are among the most threatened forests on a global scale. According to Duke et al. (2007) the planet has lost around 3.6 million ha of mangroves since 1980 corresponding to 20 % of the total area. If this unfortunate trend continues, mangroves will go extinct by 2100.

However, mangroves have extraordinary high rates of primary productivity, they function on the one hand as an atmospheric $CO_2$ sink and on the other hand as an essential source of oceanic carbon. Mangroves, including associated soils, could sequester approximately 22.8 million metric tons of carbon each year.

Covering only 0.1 % of the earth's continental surface, the forests account for 11 % of the total input of terrestrial carbon into the ocean and 10 % of the terrestrial dissolved organic carbon (DOC) exported to the ocean. The rapid disappearance and degradation of mangroves could have negative consequences for transfer of materials into the marine systems and influence the atmospheric composition and climate, because resultant gas emissions may be very high (Giri et al., 2011).

## 1.6 The Sinú River Delta Development

The Cispatá bay area has changed during the last 330 years because of several environmental and climatic causes. Mainly, the position of the Sinú river delta has changed, but also the sea level (Castaño et al., 2010). Between 1938 and 1945, the Sinú river changed its course and started a new delta at a site known as Tinajones. Earlier, in 1762, the river ran east near the coast, followed the trend of the Mestizos spit (Fig. 5) and formed a delta at the end. The spit enclosed a small body of water (Cispatá bay), where crevasse channels from the river switched part of Sinú's sediments. Between 1762 and 1849, the river deviated its entire course through one of the crevasse channels and abandoned its delta at Mestizos spit. This zone was then subjected to marine-water intrusion. The spit was eroded, and the area of Cispatá bay was reduced by 20 %. The maximum sediment accumulation occurred in front of the 1849 delta and maximum erosion occurred to the northeast, especially at the bay's mouth.

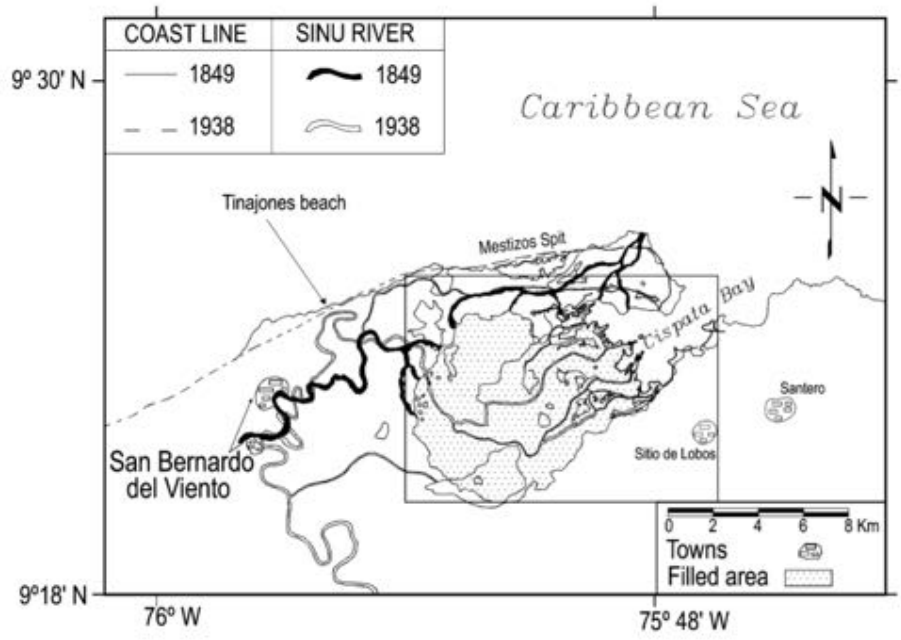


*Figure 5: Initiation of the Sinú river delta at Cispatá bay at 1849 and 1938. The currents indicate the sediment transport towards the bay (Suarez, 2004)*

Between 1849 and 1938, Cispatá bay was almost completely filled, and the Sinú river delta became a complex of channels and swamps. Maximum sedimentation occurred inland, and only a small accumulation occurred at the submarine part of the delta. By 1938, outside the filled bay, the river changed to a sinuous course and meandered near Tinajones Beach (Fig. 5). Similar to the way the process of abandonment and initiation of a new delta occurred between 1762 and 1849, the initiation of a new delta at Tinajones involved the abandonment of the delta at Cispatá bay. According to Suarez (2004), an avulsion occurs if a river bed is super-elevated above its surroundings. This result seems to have occurred at Tinajones and may describe the situation between 1762 and 1849. The delta at Tinajones thus was a result of a natural process, not of an anthropic intervention, as is sometimes believed. Today, maximum accumulation at Tinajones occurs in front of the delta, both inland and at the marine portion, especially to the west. Erosion occurs towards the east (Fig. 6).

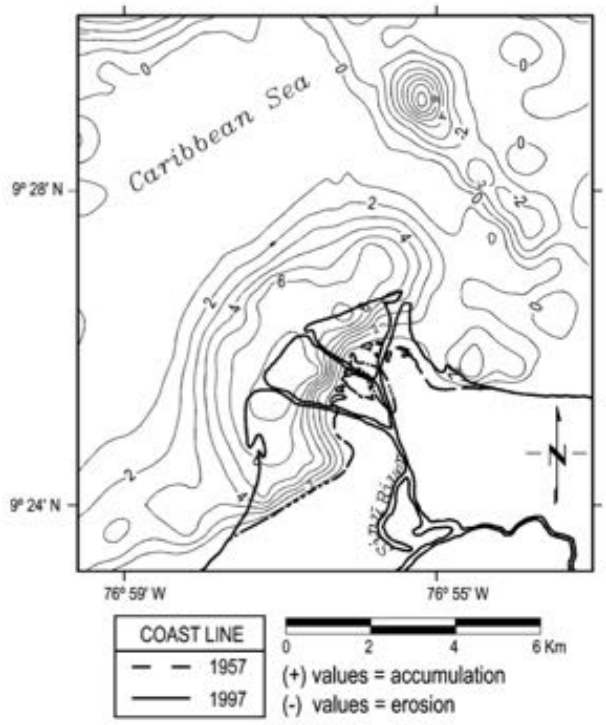


*Figure 6: Todays initiation of the Sinú river delta at Tinajones (Suarez, 2004)*

## 1.7 Structure And Tectonics Of The Sinú-San Jacinto Area

Geologically, the Sinú river delta and Cispatá bay are located in the Sinú-San Jacinto basin, which is a Paleocene to Oligocene accretionary wedge floored by Cretaceous oceanic crust (Flinch, 2003). To the southeast towards the Lower Magdalena Valley it is bounded by the Romeral fault system, to the west by the Uramita fault and to the northwest by the South Caribbean marginal fault (Fig. 7).

The Romeral fault is a major strike-slip fault that offsets the obduction suture. The Sinú-San Jacinto area is the onshore part of the northern Colombia accretionary prism, related to the subduction of the Caribbean plate underneath the South American plate.

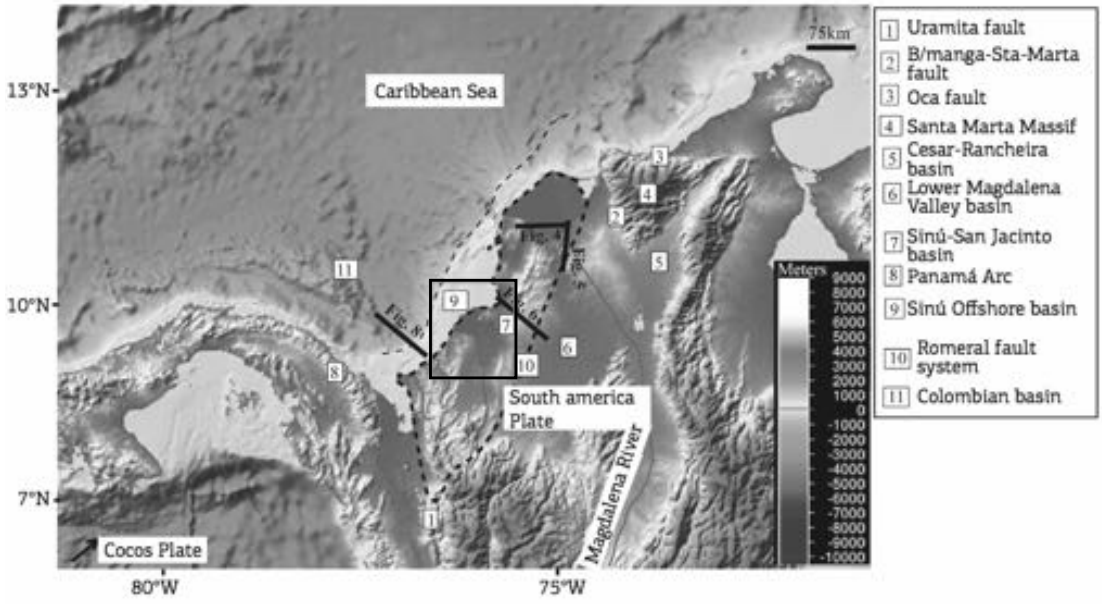


*Figure 7: Structure and tectonics of the Sinú river delta (black square), (Alfaro and Holz, 2014)*

Gravity and magnetic modelling predict a northwest-dipping (8° to 11°) crystalline basement beneath the wedge providing a rigid backstop or buttress (Kellogg et al., 2005). The Sinú-San Jacinto area can be divided into seven stratigraphic stages: First stratigraphic stage is characterised by continental to restricted marine deposition during a Triassic/ Jurassic rifting. Second, third and fourth stages correspond with deposition of a wide carbonate platform in the Cretaceous, a sandy carbonate platform during the Paleocene, and carbonate and coarse-grained fluvial sedimentation during the Eocene, respectively. Another stage is characterised by rising of base level and deep-water deposition (turbidites and pelagic/ hemipelagic sediments) during the Oligocene. The early to middle Miocene is characterised by shallow marine to fluvial sedimentation during falling base level, which is controlled by episodic events of tectonic inversion. During the late Miocene to recent, the sedimentation consists of terrigenous coarse-grained deposits (mostly of flysch-type deposits) (Alfaro and Holz, 2014).

# 2 Materials And Methods

Figure 8 shows an overview of the different steps and the order of the practical processes. Each following subsection of this part explains the individual procedures.

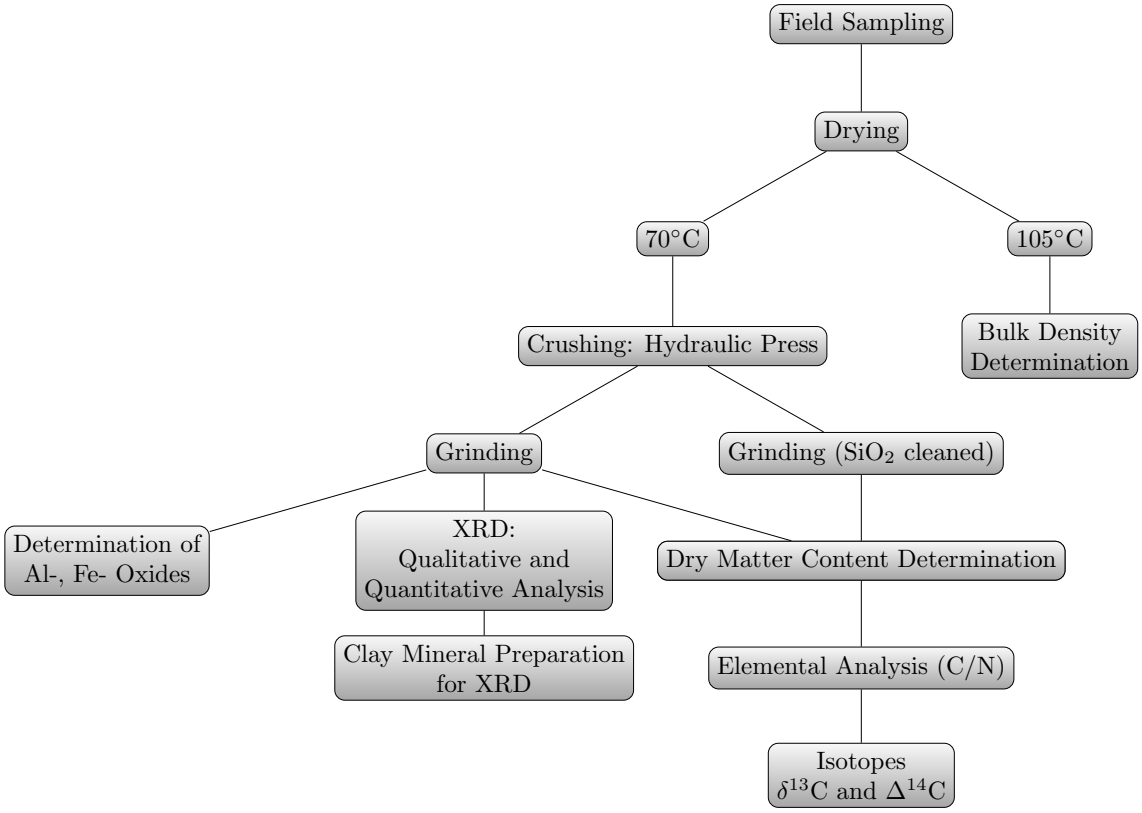


*Figure 8: Steps of sample preparation*

## 2.1 Study Site And Soil Sampling

The study site is located on the northwestern Caribbean coast in Colombia. It is situated in Cispatá Bay, which is part of the southern extreme of Morrosquillo gulf. Scenically, the coastal zone is characterised by the Sinú river delta and a complex estuarine lagoon system. Extensive wetlands and mangroves dominate this area. The Sinú river, which has changed its flow direction in the last decades,

has its origin in the northern part of the western Andes Cordilleras.

The mangrove area already contains 21 permanent plots for scientific purpose. For this research, 10 of these plots were sampled from March 12 to 13, 2016, using a soil corer with 7 cm in diameter. Owing to the wetland along the coastline, access to the plots was only possible using a boat. Five soil cores were taken at the fringe mangrove plots (P21, R1, R4, R5, R6) as well as 5 soil cores at the basin mangrove plots (P16, C1, C2, C3, C4). Generally the water table in the boreholes increased quickly after sampling. Figure 10 shows the location of the sampling points along with the deepest sampling depth. In addition to the 10 plots sampled at the mangrove forests, 3 nearby sand cores at Nispeyal coast were collected, and also 3 riverbed cores of the Sinú river in the city of Montería (compare red sample point in Fig. 9). Because those 3 plots were collected close together they show up as 1 point on the map. Generally, cores without layer changes were divided into sections every 20 cm. Conspicuous layer changes were divided at the boundary. A replication of the whole bore was necessary if the corer only sampled water beyond a certain depth. Plot C4 was divided into sections every 10 cm for eventual $\Delta^{14}C$ analysis. Table A (appendix) shows a list of all extracted sampling points and each segmental division. Because only the general mineralogical and elemental composition of the sand and river samples is important - they are considered here as end members - those samples were not divided into segments. Instead, the whole cores down to 100 cm were used as individual samples. After being collected, soil samples were properly packaged, labelled and stored.

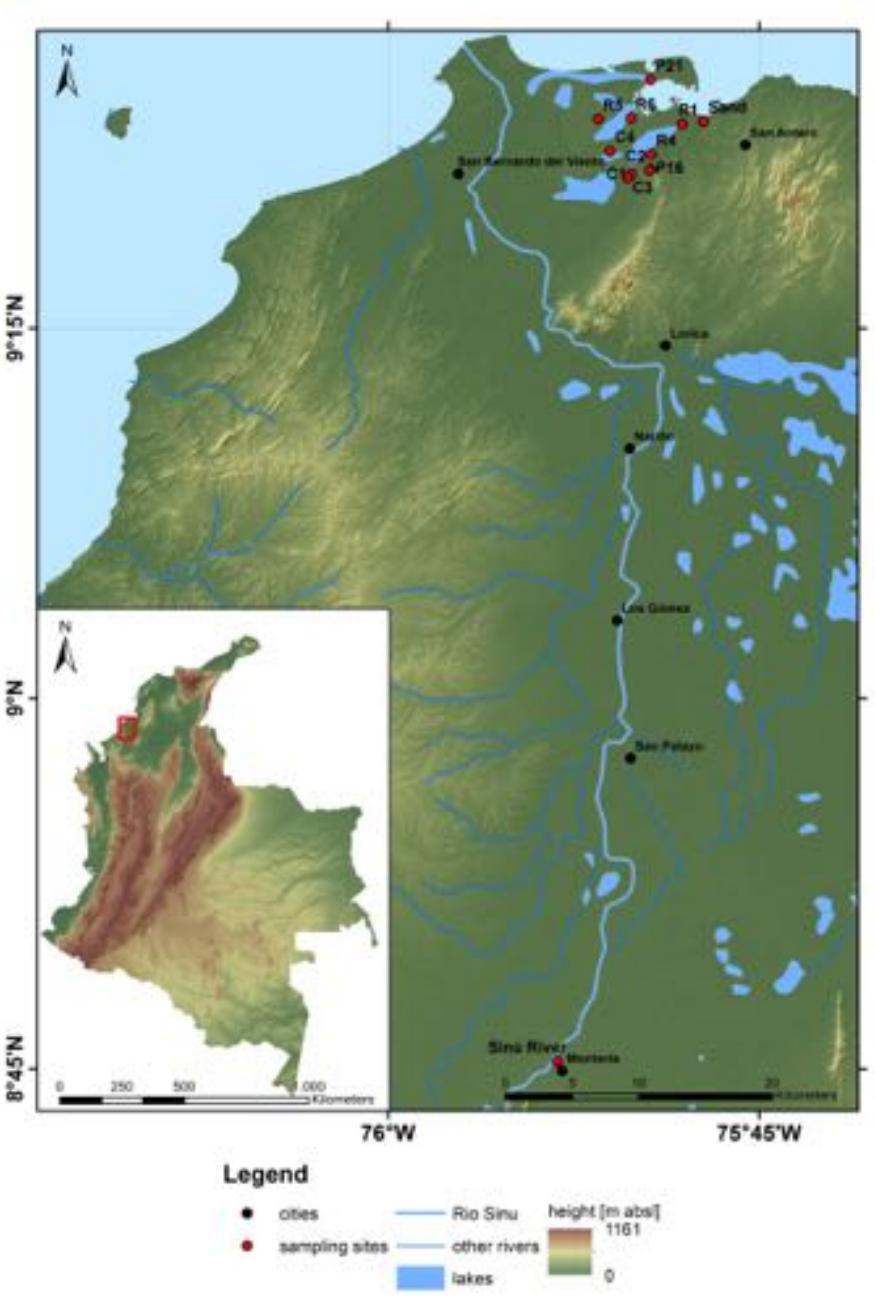


*Figure 9: Sampling points in Cispatá Bay and Montería (southern point) ArcGIS-source: http://www.diva-gis.org/gdata; accessed on June 07, 2016*

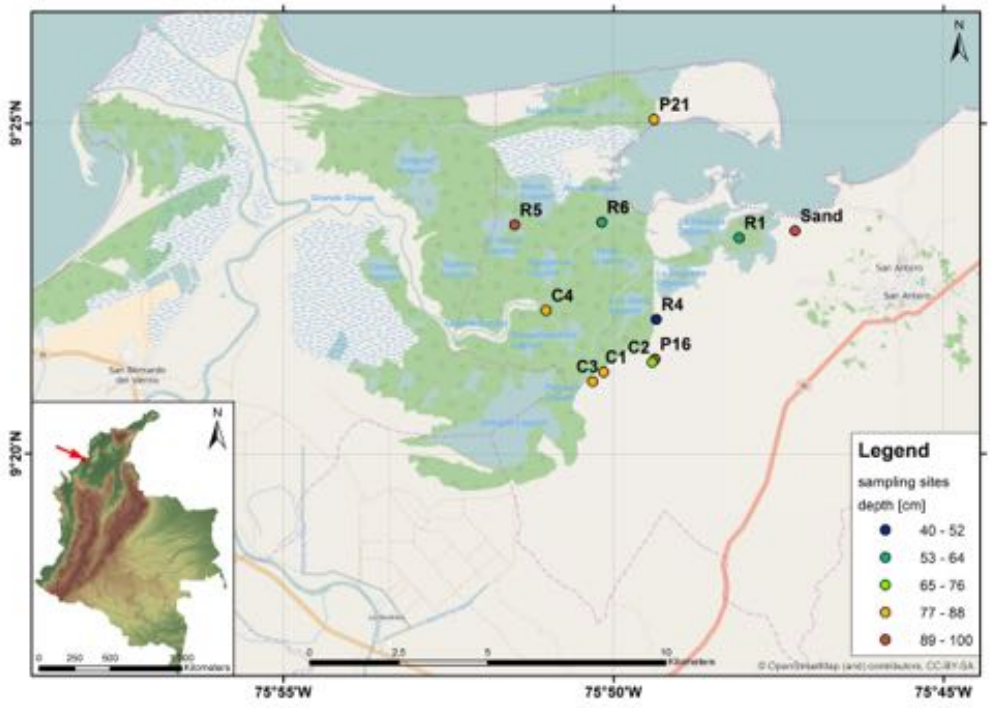


*Figure 10: Mangrove area (green) with sampling points and each deepest sampling depth (ArcGIS-map: SRTM 1Arc v3)*

All sampled fringe forest soil cores consisted almost exclusively of organic material, e.g. wood residues, leaf debris and roots. In deeper sections (below 40 cm) this humus layer was moderately decomposed and had a musty smell. Fringe forest cores showed a high water content in all sections. Layer changes were not visible except for some changes of colour from dark brown to red brown (compare soil profiles in appendix B). In contrast to those described samples, plot R1 and R5 of the fringe forest changed into a clearly visible greyish layer with a less organic content beyond 25 cm (R1) and 40 cm (R5). Together with the colour change these sections were more compact and looked more homogeneous. The finger test showed that this soil consisted primarily of silty, slightly of clayey components traversed by some thin roots. The soil was soft cohesive and moderate to easy malleable.

Basin mangrove cores showed completely different soil profiles, but they also contained much water. Collected samples were very compacted and the musty smell during sampling suggested, that the soil was low in oxygen. Samples consisted almost exclusively of silty, slightly clayey components and some roots (compare Fig. 11). All soil cores had a greyish, less brownish colour except C1, which had a consistently beige-yellow colouring. Only 3 basin plots (P16, C3, C4Rep) showed humus layers - P16 up to 30 cm, C3 up to 20 cm and C4Rep up to 10 cm. The remaining basin mangrove cores contained instead a thin organic surface layer with leaf debris and rooted young mangrove trees.


*Figure 11: First sections of plot C4-Replication showing humus and silty layers*

The additional collected sand cores from Nispeyal beach were mainly composed of broken shells and dead corals. Therefore those samples should almost exclusively consist of carbonates. The last collected soil cores in the city of Montería showed a similar composition to the basin mangrove plots. They consisted also mostly of silty, slightly sandy components but without roots.

In addition to the soil sampling, one fringe and one basin mangrove plot (P21 and C4) were selected to measure bulk density. In order not to disrupt those

collected samples, a site located approximately 2-3 m from the border of each plot was picked. In each site, a soil pit was dug and samples were collected using sampling rings with a volume of 98.52 $cm^3$. Four depth levels per plot P21 (0-20, 20-40, 40-60, 60-80 cm) were collected and five depth levels (+ 80-100 cm) for plot C4. The sampling for bulk density was replicated three times for each depth level. Altogether, the field sampling resulted in 60 soil samples out of the mangrove area, 6 end-member samples and 27 samples for the bulk density determination.

## 2.2 Drying Process

For laboratory analyses, the soil samples had to be completely dry. On the one hand laboratory methods like grinding and weighing are only possible with an anhydrous substance. On the other hand analytical results are calculated from the dry weight of the soils. Especially bulk density samples need a water content of nearly zero percent to provide conclusions for each plot area.

The extremely moist and heavy samples had already been pre-dried in Colombia to cut down the cost of shipping to Germany. They were dehumidified at 70°C at the *National University of Colombia at Medellín* for approximately 3 days (March 15 to March 18, 2016). After the arrival at the MPI-BGC in Jena on April 08, 2016 the soils were oven dried again for 5 days at 70°C. Also bulk density samples were oven dried at 105°C to get them completely dry. Each sample lost about 9 to 10 g of water on the first day and continually less water the following days (see the recording of water loss in appendix C). It took 19 days of drying until the bulk density samples obtained a constant weight.

## 2.3 Grinding

Before each of the 66 samples could be ground separately with the ball mill (type: *Retsch MM 400*), it had to be crushed using the hydraulic press. This was neces-

sary because the samples got very compacted while drying. In preparation for the grinding process, the grinding cup had to be filled up to 2/3 with sample material (1 cm free space from the top edge for the grinding ball). The ball was placed on the top of the sample material and the grinding cup was fixed in the clamping device. Two samples could be ground in parallel. The actual grinding process had a duration of 3 min with a frequency of 25 Hz for each sample. It was important not to grind the samples for too long, because this would heat up the grinding cup and carbon compounds could be lost. After grinding, the received sample amount was placed into a new plastic bag. The cups and balls were cleaned with distilled water and dried with compressed air.

For $\Delta^{14}C$ analyses, a special cleaning of the cups and balls was necessary to remove contaminations of previous grinding processes. In this case, cups including the ball had to be filled with sea sand. The following grinding process of the sand took a duration of 5 min at 30 Hz. After removing the sand, the sample could be ground using this cup.

## 2.4 Weighing And Calculation Of Dry Matter

The analytical results of the elemental C/N-analysis (see chapter 2.5) are related to the weights of the pre-dried soil (=PD: dried at 70°C). In contrast, further chemical analyses (e.g. isotope- determination, Al- and Fe-oxide contents) are related to the absolutely dry weight of the soil (=DW: dried at 105°C). For the C/N-analysis of mineral soils, these soils have to be dried at lower temperatures, in order not to destroy highly volatile carbon compounds. However, soil particles accumulate adsorbed water on their surface again after drying. To calculate the amount of this residual water a parallel drying at 105°C is necessary.

The procedure for the dry matter determination started with the weighing of empty sample vessels for the ground material. A ground sample amount of

about 3 g was weighed into those tared glass containers (refer to Table D in the appendix). The glass containers including the sample material were placed into a drying oven at a drying temperature of 105°C. After a constant weight was reached (about 12 h) the vessels were placed into a desiccator to cool down completely. The vessels including the dried material were weighed again to subtract the amount of the first weighed empty vessels (column 6 in Table D). The dry matter content (DMC) was calculated using the following equation (Hoffmann, 1991):

$$DMC[\%] = \frac{DW_{(105°C)}[g]}{PD[g]} \cdot 100\% \tag{1}$$

$$DMC[\%] = \frac{2.88g}{3.09g} \cdot 100\% = \underline{\underline{93.496\%}} \tag{2}$$

Equation 2 shows a sample calculation with soil sample P21_0-20 of Table D. Due to the long pre-drying all samples have a high dry matter content of over 90%.

## 2.5 Elemental Analysis

C and N contents were determined at the *Routine Measurements & Analysis - Laboratory* at the MPI-BGC. Small C and N concentrations were measured using the analyser *vario MAX*, which needs high sample amount inputs to record the contents without any problems. Corresponding to this, higher C and N concentrations were measured using the *vario EL*, which records only small sample amounts. The analytical principle of the analysers works as follows:

After samples are placed in an automatic sample feeder, they are transferred into the combustion tube filled with tungsten trioxide ($WO_3$) and heated up to temperatures of 1150°C (*vario EL*) and 1100°C (*vario MAX*). When the samples

are fixed in the combustion tube, the carrier gas helium is temporarily mixed with pure oxygen. Flash combustion takes place, in case of the *vario EL* analyser primed by oxidation of the tin capsules. Once the combustion of samples is accomplished, the gas mixture flows into a reduction tube filled with copper powder (*vario EL*) and tungsten (*vario MAX*), and heats up to temperatures of 850°C (*vario EL*) and 830°C (*vario MAX*). The excess oxygen is eliminated and the nitrogen oxides are reduced to nitrogen. The gases are separated by a system similar to that of gas chromatography. Nitrogen passes through the columns without delay and is measured by the thermal conductivity detector (TCD). After the integration of the nitrogen signal, carbon dioxide is released from the adsorption column, passed to the TCD, and measured. One analysis lasts 12 to 15 min depending on the C and N content of the measured samples (Hilke, 2016).

In preparation for the measurement, a test weighing into tin capsules was conducted, to find out how much sample material was needed for a successful *vario*-analysis. According to the test weighing results, samples with a suspected high carbon content (such as organic layers) were weighed into tin capsules using a small sample amount of 20 mg. Instead, samples with a suspected low carbon content (samples of deeper layers) were weighed into ceramic pots using an amount of 250 mg. Samples with a high carbonate content were also weighed into ceramic pots with an amount of 60 mg. The weighing process into the ceramic pots was done twice because total carbon (TC) and inorganic carbon (IC) can not be measured at the same time. For TC measurements, 500 mg $WO_3$ were added on the top of the samples into the ceramic pots, because the oxide works as an oxygen-supplier if the actual oxygen transfer is too low during the combustion. For IC measurements, all ceramic pots including the samples had to be placed into a muffle furnace for 17 h at 450°C. Thereby, organic carbon compounds (OC) were destroyed and only IC could be measured. The samples for IC measurements were

also treated with $WO_3$ afterwards. It was not possible to measure OC directly, therefore it was calculated by:

$$OC = TC - IC \tag{3}$$

Because the IC content in the high organic layers should be negligibly small, IC was not determined for those samples, that were weighed into the tin capsules. Finally, TC and TN contents were corrected with regard to the absolutely dry weights (see chapter 2.4) of the samples. For this, the dry mass (DM) needed to be calculated first (results in column 8, Table E):

$$DM[mg]_{(105°C)} = \frac{DMC[\%] \cdot Weight_{C,N}[mg]}{100[\%]} \tag{4}$$

Subsequently, C and N contents were corrected using this equation (Hoffmann, 1991):

$$C,N[\%]_{(105°C)} = \frac{C,N[\%]_{(70°C)} \cdot Weight_{C,N}[mg]}{DM[mg]_{(105°C)}} \tag{5}$$

The corrected TC and TN contents of the absolutely dry soil, as well as the calculations for OC are presented in Table E.

## 2.6 XRD Analysis

To get a general idea, how the mangrove area and the two end-members are mineralogically composed, the XRD measurement was conducted on 12 samples: 4 end-member samples and 4 plots of basin and fringe mangroves each. In preparation for this measurement, the ground sample amount was placed on the sample holder and the surface was levelled with pressing a glass slide on the top of the sample. It was important not to stroke the glass slide over the sample, because then minerals could have turned into a preferred orientation, what would falsify

the measurement results. Sample holders were placed in a sample stand, which was clamped into the X-ray diffractometer. Samples were measured 20 min each, from 5 to 60° 2θ.

Generally, XRD is used for qualitative and quantitative phase analyses and additionally for crystal structure refinements (*Rietveld method*). It cannot replace chemical analyses (Spieß et al., 2009). The basic principle of the XRD measurement is based on the diffraction of X-rays on planes in crystals. Because every crystalline substance has a characteristic atomic lattice, each of these substances shows an individual XRD diagram. X-rays are diffracted in crystals only if the distance of the atoms is in the same area as the wavelength of the X-radiation. X-radiation is generated between a cathode (tungsten or molybdenum filament) and an anode (copper). Thereby, electrons emitted from the cathode are accelerated to the anode due to an applied voltage. Coherent scattering of X-rays is the prerequisite for diffraction of X-rays on crystals. Coherent scattering occurs, if an electron is hit by X-rays. This causes it to oscillate, whereby it emits radiation itself. The scattering of X-rays on crystals can be interpreted using *Bragg's law*. According to Bragg, atomic planes in crystals have a constant parallel distance ($d$) to each other. On each plane, X-rays are diffracted and reflected. Because incident radiation and diffracted emerging radiation have the same angle to the plane, $d\ sin\ \theta$ is multiplied by 2 in the equation. Constructive interference occurs, when the path length difference between two planes is an integer multiple of the X-ray wavelength ($\lambda$). Therefore, $n$ (natural number) = 1.

$$n\ \lambda = 2\ d\ sin\ \theta \tag{6}$$

The radiation, that is diffracted onto the sample powder surface gets passed to a detector. A goniometer measures the radiation intensity and stores this information digitally. Using this information, a powder diffractogram is produced

including the scan along the diffraction cones. Usually, diffractograms are evaluated manually using PDF software.

Because ground sample materials include various mineral orientations, it is very likely, that single crystals are so oriented, that they diffract in the angle of 2θ opposite to the primary beam. However, clay minerals show a preferred orientation due to their structure. Thus, a different preparation of that mineral fraction was conducted:

The clay mineral analysis was performed on 8 selected representative samples including fringe and basin samples as well as two end-member samples of the Sinú river. It was not performed on the sand samples of Nispeyal because, of course, they do not contain clays. The preparation for the measurement, which consists of the clay fraction separation from the original soil, was implemented at the soil preparation laboratory at the IGW Jena: Ground sample material and deionised water are brought into suspension, whereby the mineral separation occurs. While coarse particles settle on the ground, finer particles remain in the suspension. For clay measurements, only the 2 µm grain fraction was separated from the soil using an *Atterberg-cylinder*. The cylinder was filled with 5 g of the sediment fraction smaller than 63 µm, 20 g of $Na_4P_2O_7$ (works as a dispersant and prevents the coagulation of clay minerals) and deionised water. The actual separation of clays occurred by temporal determination of the particles drop height in the suspension using an assumed density of 2.6 g/cm$^3$. Thereby, particles dropped at different speeds, depending on their grain size. This step was repeated 3 times until a sufficient amount of the 2 µm grain fraction was separated. This separation was centrifuged, the excess water was strained and the sediment mixed with the remaining water. Ceramic panels were placed onto a suction cup and an amount of 15 mg/cm$^2$ of the clay suspension was applied on their surface using a pipette. The ceramic panels, which have a diameter of 23 mm and a surface area of 4.15 cm$^2$,

have emerged as the best carrier material, because they have large pores and capillary suction. Using a vacuum applied by a water jet pump onto the suction cup, the moisture could get pulled out of the ceramic panels. Due to this process, flaky clay minerals get soaked up onto the ceramic in a static spread orientation,
490 without a parallel adjustment (Jasmund and Lagaly, 1993).

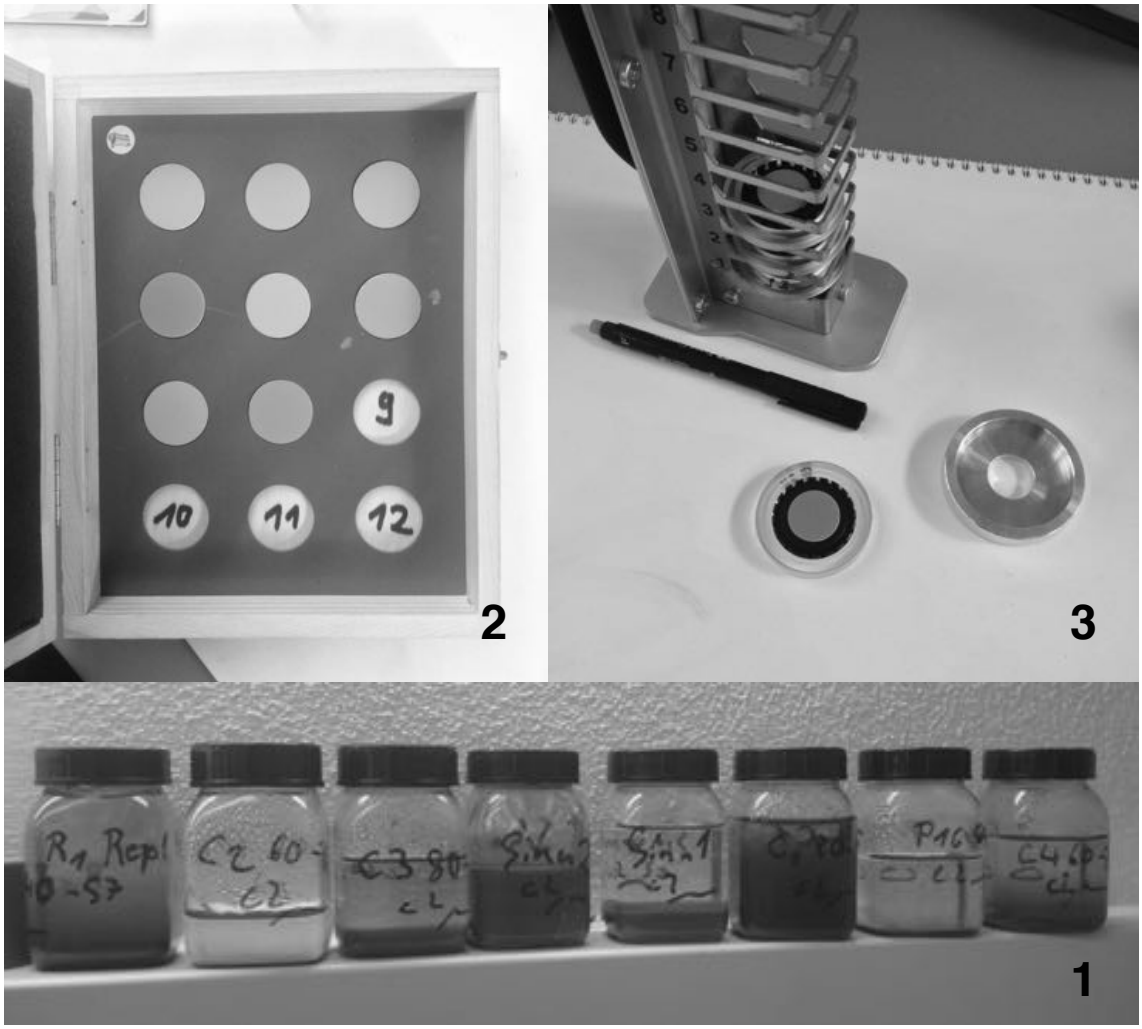


*Figure 12: Preparation of the clay fraction for XRD measurements. 1- separated clay fraction 2- clays applied onto the ceramic panels 3- insertion of the panel into the rack*

The ceramic panels were placed in an adapted rack and measured from 3 to 70° 2θ using XRD. Afterwards, samples were placed into a desiccator and steamed

with $C_2H_6O_2$ for 24h. Ethylene glycol has emerged as the best steaming device, because it widens the interlayers and, in contrast to water as steaming medium, evaporates slower. After steaming, samples were measured again from 3 to 30° 2θ. Then they were heated at 550°C for 2h and measured for the last time up to 30° 2θ. XRD powder data was refined with Rietveld program Topas, Bruker AXS.

## 2.7 Determination Of $\delta^{13}$C Signatures

Isotope Ratio Mass Spectrometry (IRMS) is a specialised technique used to provide information about the geographic, chemical, and biological origins of substances. The ability to determine the source of an organic substance stems from the relative isotopic abundances of the elements which comprise the material. Because the isotope ratios of elements such as carbon can become locally enriched or depleted through a variety of kinetic and thermodynamic factors, measurement of the isotope ratios can be used to differentiate between samples which otherwise share identical chemical compositions.

Weighing for the IRMS measurement was conducted using the *MX5* microbalance of the company *Mettler Toledo*. A small sample amount depending on the previously measured TC content (compare table 3) was weighed into small tin capsules, which have a capacity of 0.07 ml. Additionally, the standards ali-j3 (0.07 mg) and caf-j3 (0.1 mg) as well as blank capsules were weighed and placed into a capsule tray.

*Table 3: TC depending weighing recommendations for $\delta^{13}C$ determination. Coloured rows: Weighing-in for standards caf-j3 (49.44 %C) and ali-j3 (71.09 %C)*

| Carbon content | weighed portion in mg | | | |
|---|---|---|---|---|
| **C in %** | **without dilution** | **dil 1-8** | **dil 1-16** | **dil 1-32** |
| 0.5 | 10 | 40 | 50 | |
| 1 | 5 | 20 | 40 | |
| 3 | 1.67 | 6.68 | 13.36 | 26.72 |
| 5 | 1 | 4 | 8 | 16 |
| 10 | 0.5 | 2 | 4 | 8 |
| 15 | 0.33 | 1.32 | 2.64 | 5.28 |
| 20 | 0.25 | 1 | 2 | 4 |
| 25 | 0.2 | 0.8 | 1.6 | 3.2 |
| 30 | 0.17 | 0.65 | 1.36 | 2.72 |
| 35 | 0.14 | 0.56 | 1.12 | 2.24 |
| 40 | 0.13 | 0.52 | 1.04 | 2.08 |
| 45 | 0.11 | 0.44 | 0.88 | 1.76 |
| 50 | 0.1 | 0.4 | 0.8 | 1.6 |
| 60 | 0.08 | 0.32 | 0.64 | 1.28 |
| 70 | 0.07 | 0.28 | 0.56 | 1.12 |
| 80 | 0.06 | 0.24 | 0.48 | 0.96 |
| 90 | 0.056 | 0.22 | 0.45 | 0.9 |
| 100 | 0.05 | 0.2 | 0.4 | 0.8 |

The weighed sample portion was measured at the *Stable Isotope Laboratory* of the MPI-BGC using a *Finnigan MAT IRMS* coupled with an *EA 1100* elemental analyser. EA-IRMS is a bulk measurement technique, which provides representative data for the average isotopic signal of the entire sample: For determination of $^{13}C$ the bulk material must first be converted to pure $CO_2$ to permit analysis by IRMS. In this technique, samples, which were placed into the tin capsules, are loaded into an automatic sampler. They are then dropped into a combustion furnace held at 1000 °C where they are combusted in the presence of an excess of oxygen. The gaseous products of combustion are swept in a helium stream over a $Cr_2O_3$ combustion catalyst, CuO wires to oxidise hydrocarbons and silver wool to remove sulphur and halides. The resultant gases ($N_2$, $NO_x$, $H_2O$, $O_2$, and $CO_2$) are then swept through a reduction stage of pure copper wires held at 600°C. This removes any remaining oxygen and converts $NO_x$ gases to $N_2$. Water is removed by a magnesium perchlorate trap, while removal of $CO_2$ is available using a selectable trap. Nitrogen and carbon dioxide are separated by a

packed column gas chromatograph held at an isothermal temperature. The resultant chromatographic peaks sequentially enter the ion source of the IRMS where they are ionised and accelerated. Gas species of different mass are separated in a magnetic field and simultaneously measured by a Faraday cup universal collector array. For $CO_2$, masses 44, 45 and 46 are monitored (Muccio and Jackson, 2009).

Isotope ratios of samples are measured relative to universal carbonate standards (VPDB or Vienna Pee Dee Belemnite, $^{13}C/^{12}C = 0.0111802$) and are reported in the delta notation ($\delta$).

$$\delta^{13}C[‰] = (R_{sample}/R_{standard} - 1) \cdot 1000 \quad (7)$$

The value $R_{sample}$ is the abundance ratio of the minor, heavier isotope of the element to the major, lighter isotope ($^{13}C/^{12}C$). Most analysed substances are depleted in the heavy-isotope relative to the standard and will therefore have negative delta values. Ali-j3 (Acetanilide-Jena3) and Caf-j3 (a caffeine sample from a 'Traube synthesis' in larger supply) were chosen as internal working standards at the MPI-BGC: Caf-j3, because it is off the usual $\delta^{13}C$ values for $C_3$-plants by about -20 ‰ and Ali-j3, because it has an accepted $\delta^{13}C$ value of -33.94 ‰ on the VPDB scale. Thereby the offset of measured samples to the Ali-j3 value is used to correct all data (Werner and Brand, 2001).

## 2.8 Determination Of $\Delta^{14}$C Signatures

$\Delta^{14}C$ in samples was detected with Accelerator Mass Spectrometry (AMS) using a *3-MV Tandetron Ion Accelerator*. This dating method involves accelerating the ions to extraordinarily high kinetic energies followed by mass analysis. In the case of $^{14}C$, counting radioactive decay is a suitable method to determine its concentration. AMS allows the measurement of a very small sample quantity

between 0.4 and 1 mg carbon. After pretreatment, samples for radiocarbon dating are prepared for use in an accelerator mass spectrometer by converting them into a solid graphite form. This is done by conversion to $CO_2$ with subsequent graphitisation in the presence of a metal catalyst. However, burning the samples to convert them into graphite, also introduces other elements into the sample like $^{14}$N. When the samples have finally been converted into graphite, they are pressed onto a metal disc. Reference materials are also pressed on metal discs. These discs are then mounted on a target wheel, so that they can be analysed in sequence. Ions from a caesium gun are then fired at the target wheel, producing negatively ionised carbon atoms. These C atoms pass through focusing devices and an injection magnet before reaching the tandem accelerator where they are accelerated to the positive terminal by a voltage difference of 2500 kV. At this stage, other negatively charged atoms are unstable and cannot reach the detector. The negatively charged C atoms, however, move onto the stripper (a gas or a metal foil) where they lose the electrons and emerge as the triple, positively charged C atoms. At this stage, molecules that may be present are eliminated because they cannot exist in this triple charged state. The C atoms with triple positive charge, further accelerate away from the positive terminal and pass through another set of focusing devices where mass analysis occurs. In mass analysis, a magnetic field is applied to these moving charged particles, which causes the particles to deflect from the path they are traveling. If the charged particles have the same velocity but different masses, as in the case of the C isotopes, the heavier particles are deflected least. Detectors at different angles of deflection then count the particles. Stable isotopes are measured by the current of the ion beam. Thereby the beam is adsorbed in a Faraday cup. At the end of an AMS run, data gathered is not only the number of $^{14}$C atoms in the sample but also the quantity of $^{12}$C and $^{13}$C. From these data, concentration ratio of the isotopes can be known to allow evaluation of the level

of fractionation. Correcting for mass-dependent fractionation is performed by a normalisation to $\delta^{13}C = -25‰$ with respect to the VPDB standard for $\delta^{13}C$. In the $^{14}C$ community worldwide, two primary standards are used for corrections: the standard SRM-4990B, called OX-I, and the standard SRM-4990C, called OX-II or NOX (for New OXalic acid), both distributed by NIST (National Institute of Standards and Technology). Generally, the isotopic ratio of $^{14}C$ is given as fraction of the modern $^{14}C$ isotopic ratio, denoted F (Fraction Modern or $F^{14}C$). The corresponding $^{14}C/^{12}C$ ratio of this modern $^{14}C$ isotopic ratio can be deduced from the corresponding specific activity of 13.56 ± 0.07 dpm (disintegrations per minute) $g^{-1}C$, referring to the year 1950 and the half-life of $^{14}C$ of 5730 ± 40 years. Given these values, an isotopic ratio $^{14}C/^{12}C$ of $1.18 \cdot 10^{-12}$ is calculated for a sample with 1 $F$ (Schuur et al., 2016).

According to its half-life, the oldest dates that can be reliably measured by radiocarbon dating are around 50.000 years ago. Because of the relatively rapid cycling of C between the atmosphere and living biomass, most fast-growing tissues of plants growing in pre-industrial times (before 1950) maintained a $^{14}C/^{12}C$ value equal to that of atmospheric $CO_2$, once corrected for mass-dependent isotope fractionation effects. There are two human activities recognised to have irreparably changed the global radiocarbon levels - the burning of fossil fuel and nuclear weapons testing. Burning of large quantities of fossil fuels like coal, referred as the *Suess-effect*, had significantly lowered the radiocarbon concentration of the atmospheric carbon reservoir. In contrast, nuclear weapons testing in the 1950's and 1960's dramatically increased the level of $^{14}C$ in the atmosphere. The phenomenon is referred to as the *bomb effect*. The bomb effect refers to the phenomenon that produced artificial radiocarbon in the atmosphere in unnatural quantities due to nuclear bombs. The huge thermal neutron flux produced by nuclear bombs reacted with N atoms present in the atmosphere to form $^{14}C$, which is known as

bomb carbon. Nuclear weapons testing in the 1950's and 60's have nearly doubled the tropospheric burden of $^{14}CO_2$ as measured in around 1965. The level of bomb carbon in the northern hemisphere reached a peak in 1963, and in the southern hemisphere around 1965. $^{14}CO_2$ then began to decrease rapidly as the negative isoflux from the ocean and terrestrial biosphere became larger than the positive isoflux from the stratosphere. The observed trend in $^{14}CO_2$ resembled an exponential curve, initially falling rapidly (by more than 40‰ year$^{-1}$) then slowing with time (Schuur et al., 2016). That post-bomb $^{14}C$ signatures are also marked as increasing $F^{14}C$ values for measured soil samples of Cispatá Bay is shown in section 3.2/ figure 20.

$\delta^{13}C$ and $\Delta^{14}C$ measurement results are given in table F (appendix).

## 2.9 Aluminum-Oxide And Iron-Oxide Analyses

Pedogenic crystalline and amorphous aluminum- and iron oxides were determined to figure out in which soil samples they mainly occur, and further, to draw conclusions about additional transported carbon via clay minerals. Type and quantity of pedogenic oxides were determined using selective extraction methods. Because silicates should not be involved into chemical reactions, oxalate- and dithionite extraction methods (Table 4) have proved their worth in previous studies (McKeague and Day, 1966).

*Table 4: Oxalate- and dithionite soluble oxides*

| **Abbreviation** | **Description** | **Explanation** |
|---|---|---|
| $Fe_o$, $Al_o$ | oxalate soluble Fe+Al | organically complexed, amorphous watery oxides |
| $Fe_d$, $Al_d$ | dithionite soluble Fe+Al | amorphous oxides + soluble crystalline oxides, e.g. Goethite, Hematite, Lepidocrocite, Ferrihydrite |
| $Fe/Al_{cryst}$ ($Fe_d$-$Fe_o$) | crystalline Fe+Al oxides | crystalline |

Iron and aluminium were determined in acid-ammonium-oxalate extracts (pH 3.0) and in sodium-citrate-dithionite extracts (pH 7.3). Because sodium dithionite extracts both crystalline and amorphous oxides, the oxalate extraction is necessary to extract only amorphous oxides. This reaction can only take place in a dark environment. Under light influence, photochemical reactions reduce also crystalline oxides.

*Implementation of dithionite-extractions:*

For this method, 46 samples, 1 standard soil and 1 blank were selected. Also, 0.5 g (+/−0.005 g) of each ground sample and standard were weighed into centrifuge tubes. Additionally, 0.5 g (+/−0.005 g) of solid sodium dithionite ($Na_2S_2O_4$) and 30 ml of citrate-carbonate solution were added. Blanks were only filled up with chemicals. Tubes were joggled over night (16 h) using the overhead shaker. They were centrifuged for 20 min at 3500Umin$^{-1}$ afterwards. Centrifuge supernatants were filtered out into 100 ml volumetric flasks using funnels. Centrifuge residues were fluffed up with 20 ml Millipore water, again centrifuged for 20 min and filtered out into the volumetric flasks, which were then filled up to 100 ml. One part of the finished extracts was diluted at a ratio of 1:19 with Millipore water and filled into 5 ml tubes.

*Figure 13: Dithionite extraction at the stage of the second filtering process*

The actual measurement of crystalline and amorphous iron and aluminium oxides was performed using the Inductively-Coupled Plasma Atomic Emission Spectrometer (ICP-AES) at the *MPI-BGC Laboratory For Spectrometry*. Undiluted extracts were kept cool as a backup.

The dithionite extraction works as follows: While dithionite reduces the oxides, sodium citrate has a buffering effect and causes an inner-complex binding of $Fe^{++}$, with the effect, that no hydroxide precipitation is produced (equations from Lambeth and Palmer (1973)).

$$S_2O_4^{--} + 2Fe^{+++} + 4OH^- \longrightarrow 2SO_3^{--} + 2Fe^{++} + 2H_2O$$

$$2SO_3^{--} + 4Fe^{+++} + 4OH^- \longrightarrow 2SO_4^{--} + 4Fe^{++} + 2H_2O$$

Addition of both equations and total reaction:

$$S_2O_4^{--} + 6Fe^{+++} + 8OH^- \longrightarrow 2SO_4^{--} + 6Fe^{++} + 4H_2O$$

*Implementation of oxalate-extractions:*

First, oxalate solution was produced adding oxalic acid to 0.2 mole $NH_4^+$ oxalate solution until it reached a pH-value of 3.0. Again, 46 samples, 1 standard soil and 1 blank were selected for this method. 0.5 g (+/−0.005 g) of each ground sample were weighed into opaque centrifuge tubes.

*Dark reaction*:

25 ml oxalate solution was added to the ground sample and joggled for 2 h using the overhead shaker. The mixture was then filtered out into 50 ml volumetric flasks using folded filters. Those filters were rinsed again with 20 ml Millipore water.

*Light reaction*:

Volumetric flasks were filled up to 50 ml. One part of the finished extracts was filled into 5 ml tubes. The actual measurement of amorphous iron and aluminium oxides was performed with the same spectrometer. Undiluted extracts were also kept cool as a backup (methods from Sparks et al. (1996)).The results for the aluminium-oxide and iron-oxide measurement are given in table F (appendix).

Inductively coupled plasma atomic emission spectroscopy (ICP-AES) is an analytical technique used for the detection of trace metals. It is a type of emission spectroscopy that uses the inductively coupled plasma to produce excited atoms and ions that emit electromagnetic radiation at wavelengths characteristic of a particular element. When the sample solution is introduced into the spectrometer, it becomes atomized into a mist-like cloud. This mist is carried into the argon plasma with a stream of argon gas. The plasma (ionized argon) produces temperatures close to 7000 °C, which thermally excites the outer-shell electrons of the elements in the sample, emitting light wavelengths characteristic of its elements. A mirror reflects the light through the entrance slit of the spectrometer onto a grating, that separates the element wavelengths onto photomultiplier de-

tectors. The relaxation of the excited electrons as they return to the ground state is accompanied by the emission of photons of light with an energy characteristic of the element. Because the sample contains a mixture of elements, a spectrum of light wavelengths are emitted simultaneously. The spectrometer uses a grating to disperse the light, separating the particular element emissions and directing each to a dedicated photomultiplier tube detector. The more intense this light is, the more concentrated the element. A computer converts the electronic signal from the photomultiplier tubes into concentrations. The determination portion of the process takes then approximately 2 min to complete (Raessler, 2016).

### 2.10 Statistical Analyses

The mean and standard deviation values were calculated. Differences among mangrove stands were analysed by a parametric one-way ANOVA (analysis of variance). All statistical tests were performed using R.

## 3 Results

### 3.1 Carbon And Nitrogen In Soil

Soil bulk density was calculated as dry mass divided by fresh volume, that matches the used sampling rings ($V = 98.52$ cm$^3$). The following boxplots (Fig. 14) show minimum, maximum, median and the interquartile range for calculated bulk densities of 3 replicates of each depth interval. Even though weights in Table B and therefore also bulk densities show some outliers, they increase slightly with depth for fringe samples. Instead, basin samples do not show a trend of increasing bulk density with depth. Although boxplots for basin mangroves samples show much higher interquartile ranges, it is conspicuous, that they also have much higher bulk densities in all depths, than fringe mangrove samples: While plot P21 sam-

ples only show an average bulk density of 0.16 g/cm$^3$, plot C4 samples show an average bulk density of 1.11 g/cm$^3$.

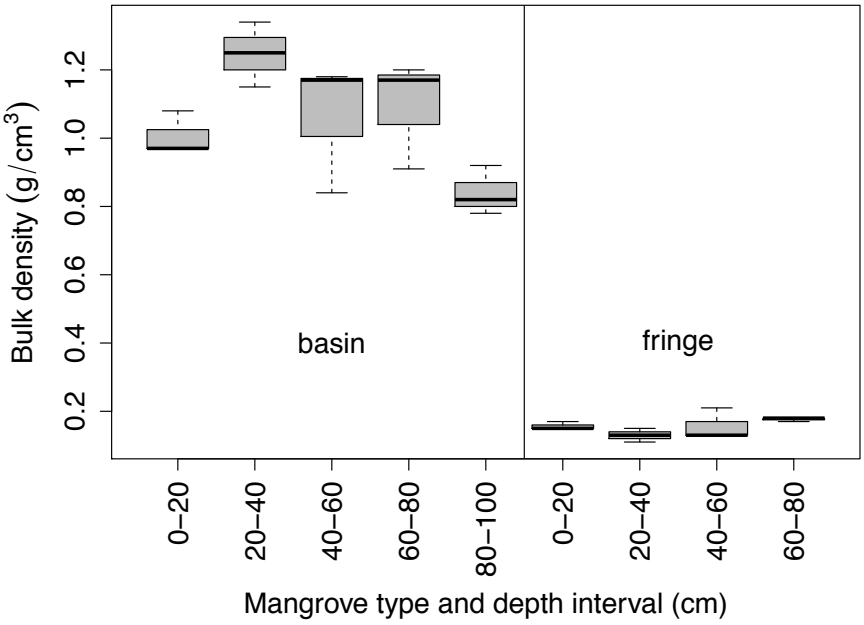


*Figure 14: Bulk densities of basin mangrove plot C4 and fringe mangrove plot P21*

The following boxplots (Fig. 15) display concentrations of OC (%OC), IC, TN and the ratio of TC/TN. The featured concentrations and the TC/TN ratio refer only to the individual plots and ignore initially the different plot depth intervals. As the figures imply, %OC and %TN differ considerably between fringe and basin mangrove soils. Soils in fringe mangroves (P21 - R6) contain much higher %OC and %TN and slightly higher TC/TN relations than those in basin mangroves (C1 - P16). Although plots C2, P16, R1, R5 and R6 show high interquartile ranges for %OC and %TN, a general difference of the mentioned parameters is noticeable between both mangrove types. The differences in %OC and %TN between basin and fringe mangrove types are significant according to the one-way ANOVA test ($p$-value <0.001). Both end-members, sampled at the Sinú river in Montería

and at Nispeyal beach, show OC and TN concentrations near zero and include therefore almost no organic compounds. In contrast, sand Nispeyal plots display the highest IC concentration of around 11 % compared to the other plots. This value is similar to the IC concentration of pure calcium carbonate (Table E).

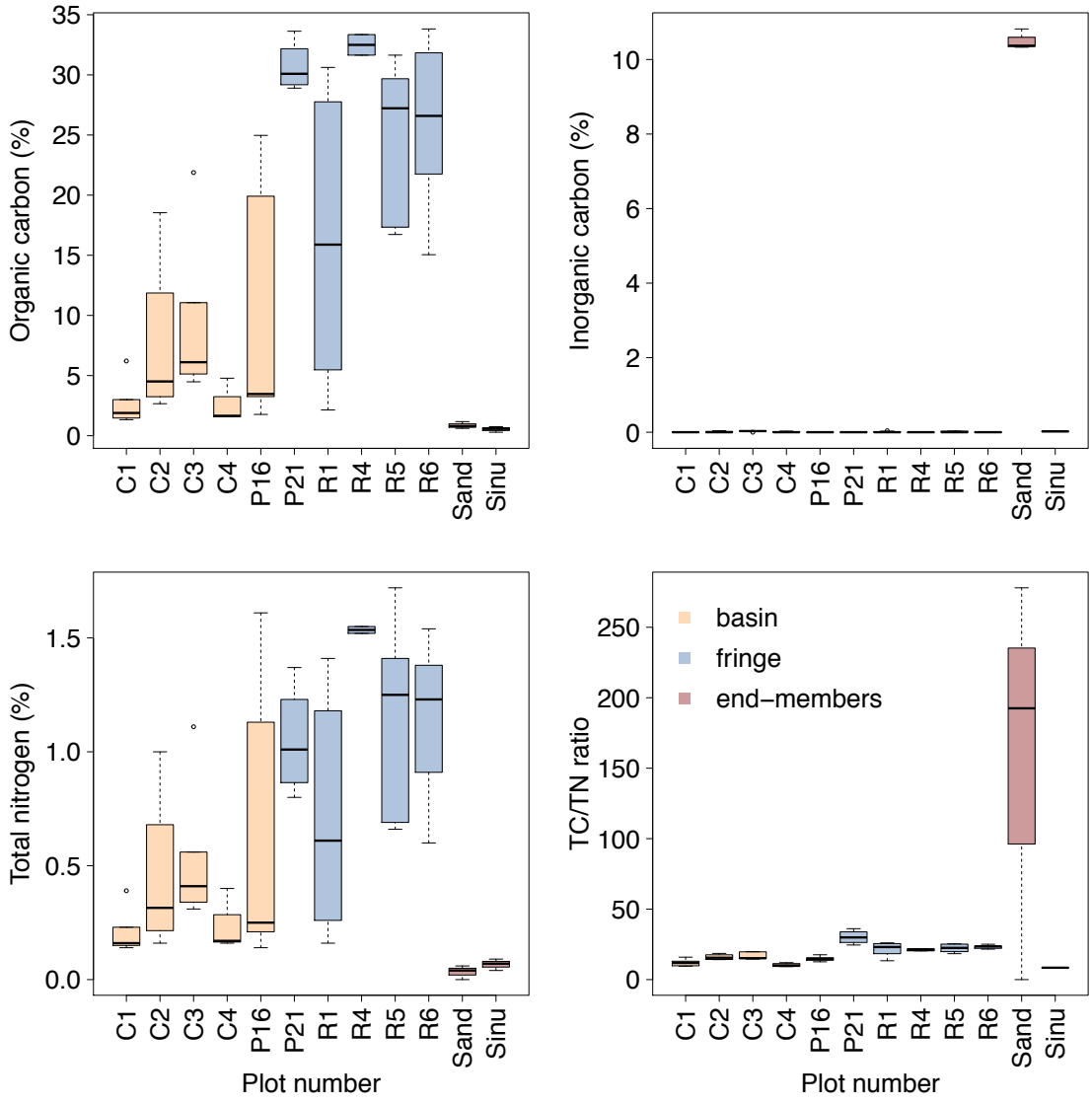


*Figure 15: OC, IC and TN concentrations as well as TC/ TN ratio depending on plot numbers*

The concentrations shown in Figure 16 refer to the merged soil depths for basin and fringe mangroves each. Again, certain depth intervals (0-20, 20-40, 40-60, 60-

725 80) show very high interquartile ranges for %OC and %TN. However, the general trend is, that %OC and %TN decrease with soil depth (see also Table E). Only plots C1 and R5 have a sudden increase of %OC in depth intervals 80-100 cm and 60-80 cm, which also changes the boxplot positions at these depth intervals. A similar increase is also shown for TN concentrations.

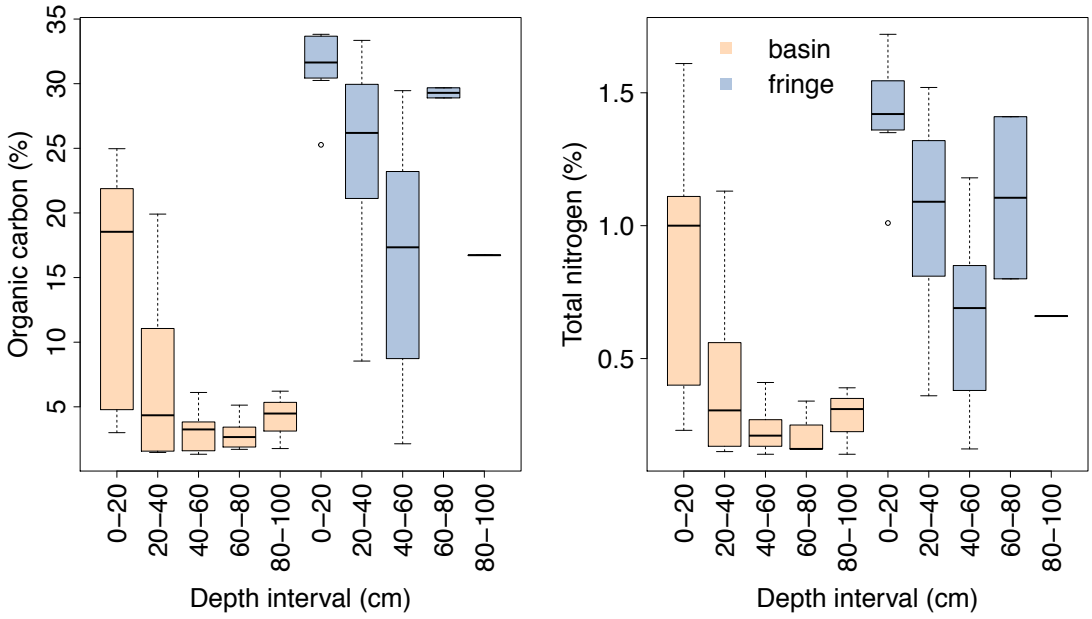


*Figure 16: OC and TN concentrations depending on depth intervals*

730 To draw conclusions about the carbon storage in both mangrove soil types, total organic carbon (TOC) was determined. TOC (megaton carbon/hectare) was calculated using the defined bulk densities of basin and fringe mangroves multiplied by plot depth intervals and %OC (see results in table 5):

$$TOC(MgC/ha) = OC\ (\%) \cdot Bulk\ density\ (g/cm^3) \cdot depth\ interval\ (cm) \quad (8)$$

*Table 5: Organic carbon, bulk density and total organic carbon by mangrove type and soil depth. Values in parentheses indicate standard deviation*

| Mangrove type | Depth [cm] | OC [%] | Bulk density [g/cm$^3$] | TOC [MgC/ha] |
|---|---|---|---|---|
| Basin | 0-20 | 14.63 (10.09) | 1.01 (0.06) | 295.61 (203.77) |
| | 20-40 | 7.12 (7.19) | 1.25 (0.10) | 161.99 (147.07) |
| | 40-60 | 3.22 (1.93) | 1.06 (0.19) | 68.35 (40.95) |
| | 60-80 | 2.96 (1.39) | 1.10 (0.16) | 65.21 (30.58) |
| | 80-100 | 4.15 (2.24) | 0.84 (0.08) | 69.78 (37.60) |
| Fringe | 0-20 | 31.32 (2.82) | 0.16 (0.01) | 100.24 (9.03) |
| | 20-40 | 23.61 (8.70) | 0.13 (0.02) | 62.79 (22.56) |
| | 40-60 | 16.12 (10.92) | 0.16 (0.05) | 51.57 (34.94) |
| | 60-80 | 29.29 (0.55) | 0.18 (0.00) | 105.44 (1.99) |

Figure 17 displays the calculated TOC contents for each depth and mangrove type. Including bulk densities to calculate TOC results in a completely different distribution of TOC compared to the previous plots. Although box plots 0-20 and 20-40 of basin mangroves show very high interquartile ranges for TOC, a higher carbon storage in the upper layers of basin mangrove soils is clearly outlined. The differences in TOC between basin and fringe mangrove types are significant according to the one-way ANOVA test ($p$-value $<0.05$). As shown in the graphs, TOC decreases with soil depth within the first four (basin) and three (fringe) layers. There is still an apparent increase of TOC in the last measured depth intervals, which is associated to higher %OC values for these layers.

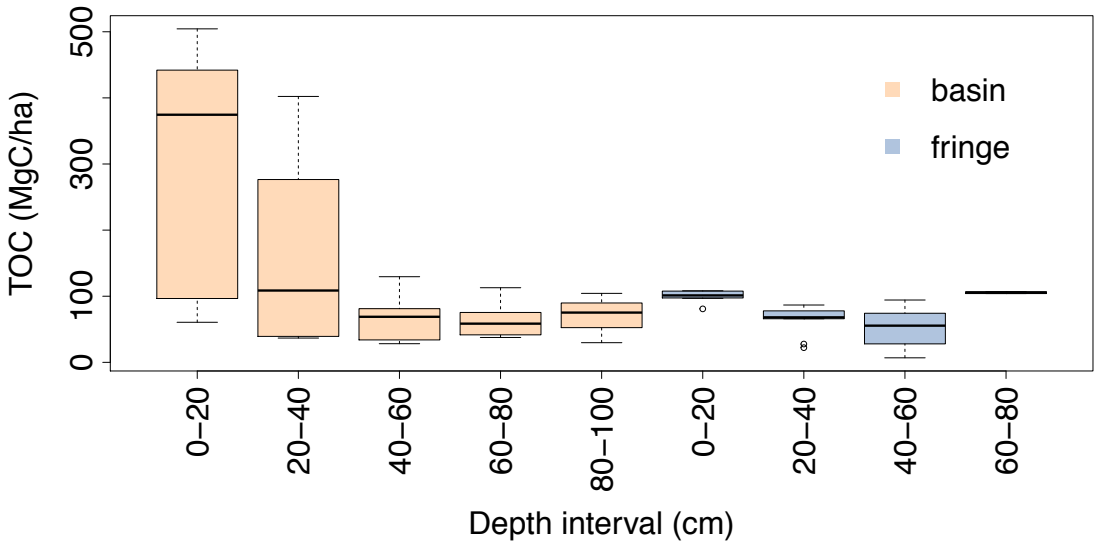


*Figure 17: Total organic carbon (MgC/ha) in basin and fringe mangroves by soil depth intervals*

## 3.2 $\delta^{13}$C And $\Delta^{14}$C Signatures

$\delta^{13}$C signatures are used as indicators for the origin of carbon in the sampled material. The negative values indicate the $^{13}C/^{12}C$ ratio and the difference to the $\delta^{13}$C VPDB standard, which is around zero (0.01118 ‰). To get informations about the origin of sediments in the mangrove forest, the two chosen end-members are useful as comparative samples. $\delta^{13}$C values for each mangrove type, both end-members and corresponding depths are displayed in Fig. 18. Strong variations in $^{13}$C are conspicuous for the depth intervals 20-40 and 40-60 cm of basin mangrove boxplots. There is no identifiable continuous trend between $\delta^{13}$C values and depth. However, differences in $^{13}$C between fringe and basin mangroves are significant according to ANOVA ($p$-value <0.001). Thus, fringe mangrove samples tend to have slightly more negative $^{13}$C values (-29 ‰) than basin mangroves samples (-27 ‰). Basin depth intervals 20-40 and 40-60 cm even show outliers with equal $\delta^{13}$C signatures to the Sinú river end-member of around -25 ‰. The less negative

values are shown by the carbonate sand end-member samples with approximately -3 ‰. This value is the closest to the $\delta^{13}$C VPDB standard with 0.01118 ‰.

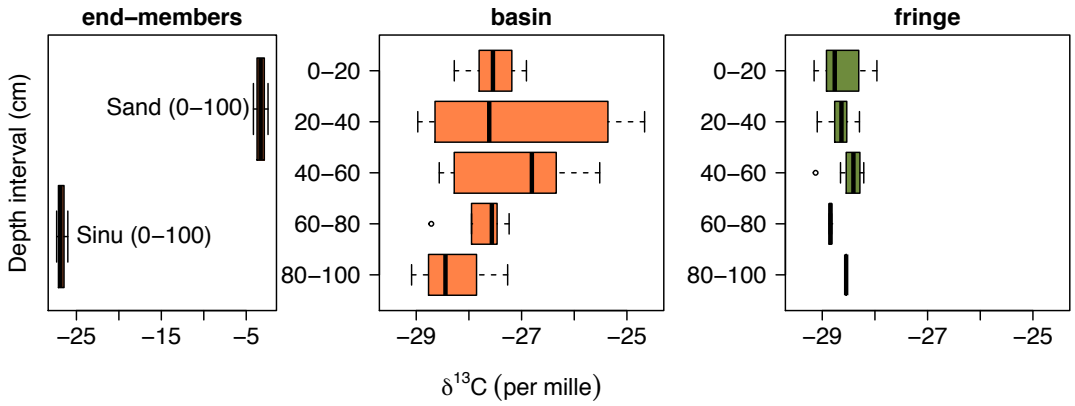


*Figure 18: $\delta^{13}C$ signatures for each depth, mangrove type and end-members*

Figure 19 shows $\Delta^{14}$C and corresponding F$^{14}$C signatures depending on each sampling depth. $^{14}$C analysis was conducted on 2 plots of basin and fringe mangroves each. As mentioned in section 2.1, plot C4 was divided every 10 cm, to figure out if isotopic signatures differ at more frequent intervals. F$^{14}$C values greater than 1, or rather positive $^{14}$C values indicate clear post-bomb signals after the year 1950. This means applied to the ages, that sample R5 is the youngest and most enriched in radiocarbon of these 4 sediment constituents, whereas C4 is the oldest (most $^{14}$C depleted). P16 and P21 are intermediate in age. In general, post-bomb fringe samples tend to be younger than pre-bomb basin samples. Although each sample with depths deeper than 70 cm is more $^{14}$C depleted than the corresponding topsoil samples at 10-20 cm, all 4 samples do not show a continuous depletion with depth.

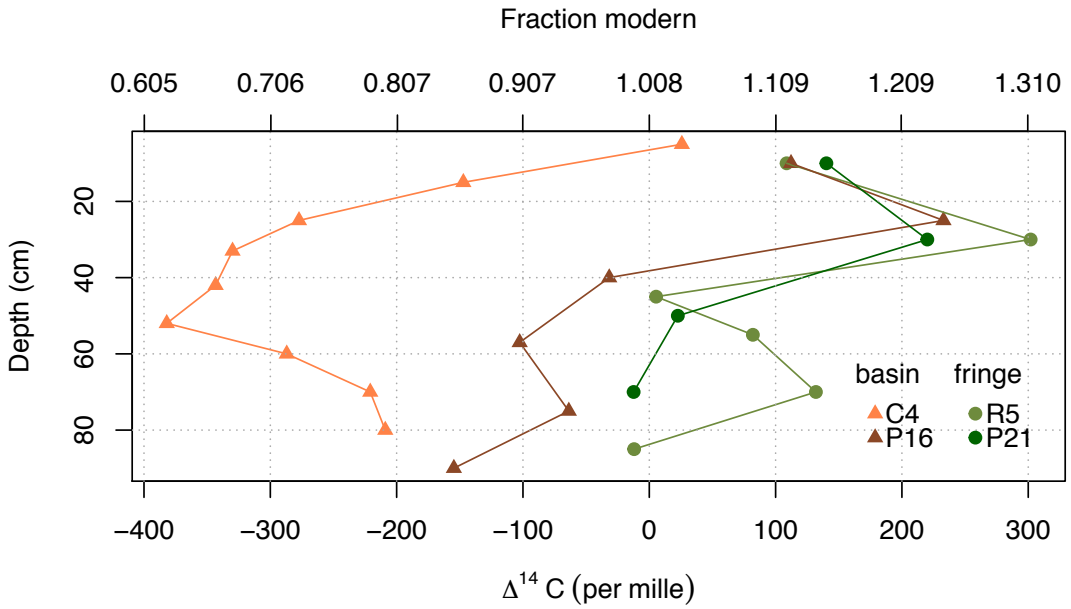


*Figure 19: $\Delta^{14}C$ and $F^{14}C$ signatures for each depth and mangrove type*

Figure 20 displays $F^{14}C$ signatures towards the corresponding years (BC, AD). Each year, which is only approximate (BC time ranges around +/−100 years), was calculated using OxCal v4.2. $F^{14}C$ values >1 indicate that the sample has more $^{14}C$ than the preindustrial atmosphere indicating again the presence of bomb $^{14}C$. A general trend showing older bottom soil and younger topsoil can be noticed. Basin mangrove samples do not show post-bomb signals. Age calculation for plot C4 resulted in ages up to 3900 years in the 47-57 cm layer. Even the topsoil of plot C4 (0-10 cm) contains older C than the other topsoil samples P16, R5 and P21 characterised by ages around 60 years compared to 20-25 years of fringe plots.

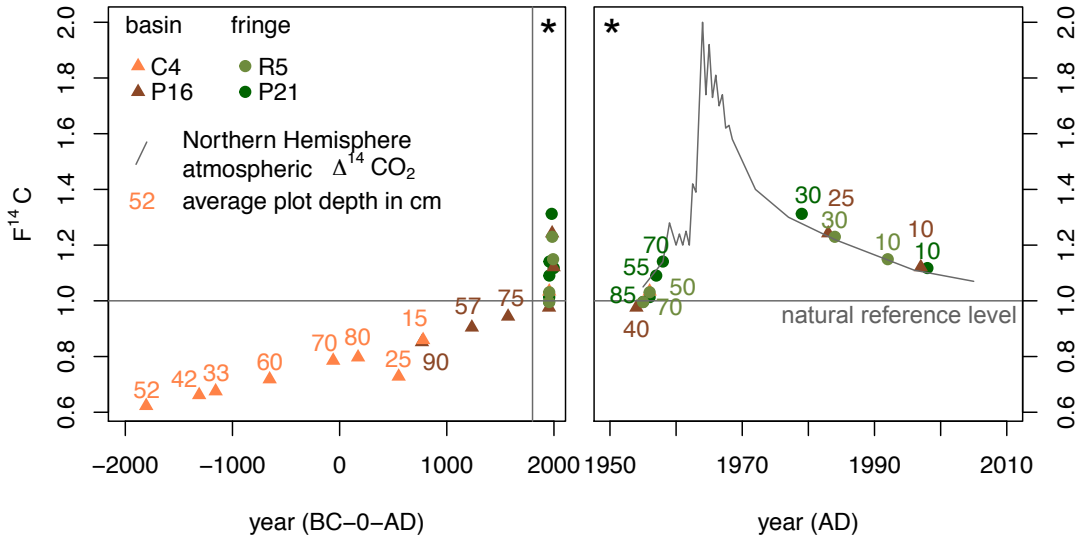


*Figure 20: $F^{14}C$ signatures and ages for each depth and mangrove type compared to the development of Northern Hemisphere atmospheric $\Delta^{14}CO_2$ in the last 60 years due to the production of $^{14}C$ by atmospheric weapons testing. Age data adapted from OxCal v4.2 (Reimer et al., 2004; Ramsey et al., 2010)*

## 3.3 Mineral Fraction Analysis

Table 6 gives an overview of the dominant crystalline phases of the studied area. In contrast to the previous results, there is no difference between basin and fringe mangroves in view of the composition of the mineral fraction. The proportion of mineral soil is bigger in basin than in fringe mangroves. Fringe mangrove soils show in contrast a higher proportion on halite than basin soils.

*Table 6: General mineralogical composition of Cispatá Bay region and Montería*

| Class | Mineral | Formula |
|---|---|---|
| Silicates | Clinochlore | $(Mg,Fe^{2+})_5Al(Si_3Al)O_{10}(OH)_8$ |
| | Illite | $(K,H_3O)Al_2(Si_3Al)O_{10}(H_2O,OH)_2$ |
| | Albite | $NaAlSi_3O_8$ |
| Carbonates | Aragonite | $CaCO_3$ |
| | Calcite | $CaCO_3$ |
| Oxides/hydrox. | Quartz | $SiO_2$ |
| Halides | Halite | NaCl |

The XRD pattern of Nispeyal samples measured from 5 to 60 °2$\theta$ shows characteristic °2$\theta$ intensities for the phases aragonite, calcite and quartz (Fig. 21), which were determined using PDF data. The XRD measurement combined with Rietveld refinement using Topas (Bruker) yielded a mineral composition of 95% aragonite, 4% calcite and 1% quartz.

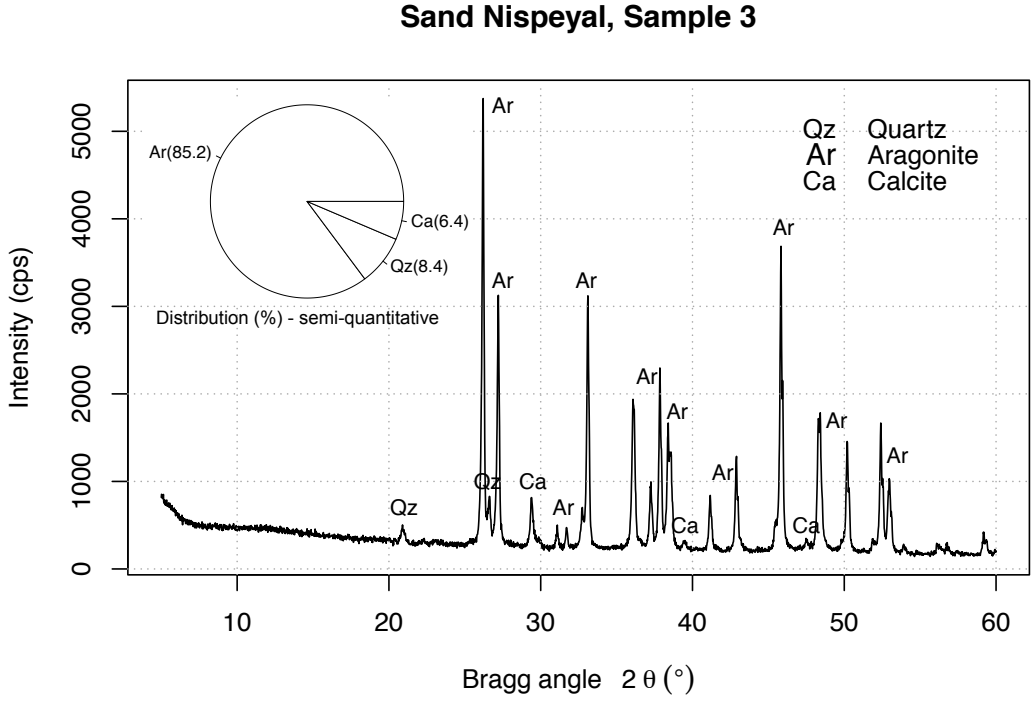


*Figure 21: XRD pattern ($\lambda$ = 1.5406 Å) of Nispeyal beach sample 3 and semi-quantitative distribution of detected minerals*

Sample 3 of the Sinú river (fig. 22) was also measured from 5 to 60 °2$\theta$. The corresponding XRD pattern shows intensities for quartz and sodium feldspar (albite) components, as well as peaks for the clay minerals illite and clinochlore. The semi-quantitative distribution seems to indicate, that quartz is the main representative of the mineral fraction of the Sinú river soils.

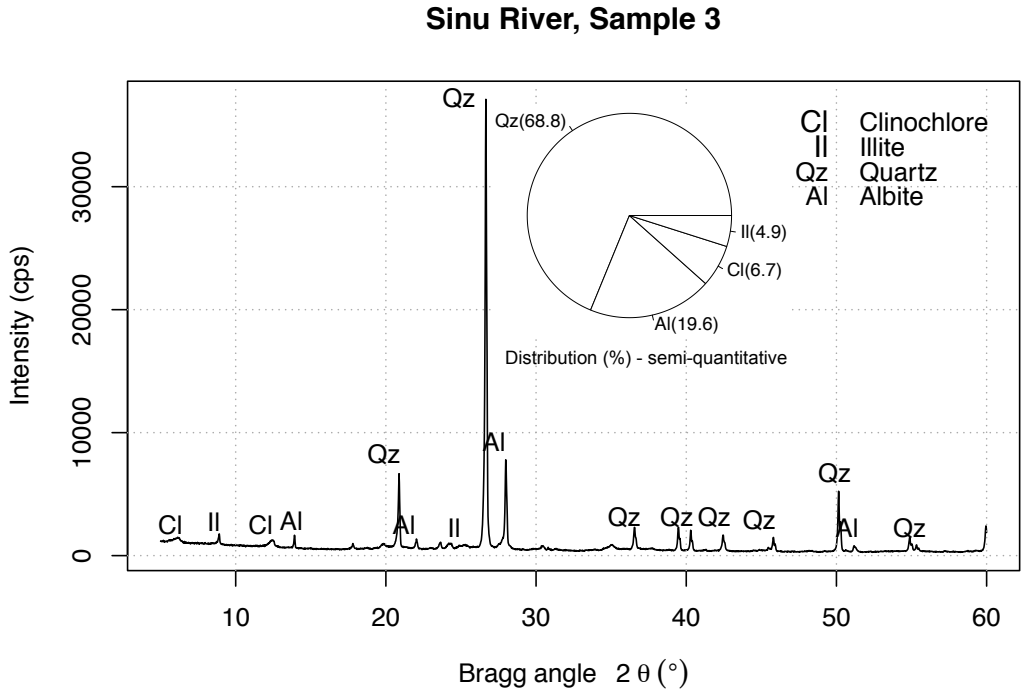


*Figure 22: XRD pattern ($\lambda$ = 1.5406 Å) of Sinú river sample 3 and semi-quantitative distribution of detected minerals*

Because the XRD patterns of the other measured plots, especially the ones of basin soils, show a similar mineralogical distribution compared to the one of the Sinú river, only two patterns (Fig. 23) were selected to show mineral contents in fringe and basin mangroves each. Plot R5 was selected, because it is the only plot which shows, next to the usual mineral phases, various high intensities for halite. Therefore also the semi-quantitative distribution contains the highest proportion on halite. Halite was also found in basin mangroves, but not in a comparable distribution ratio.

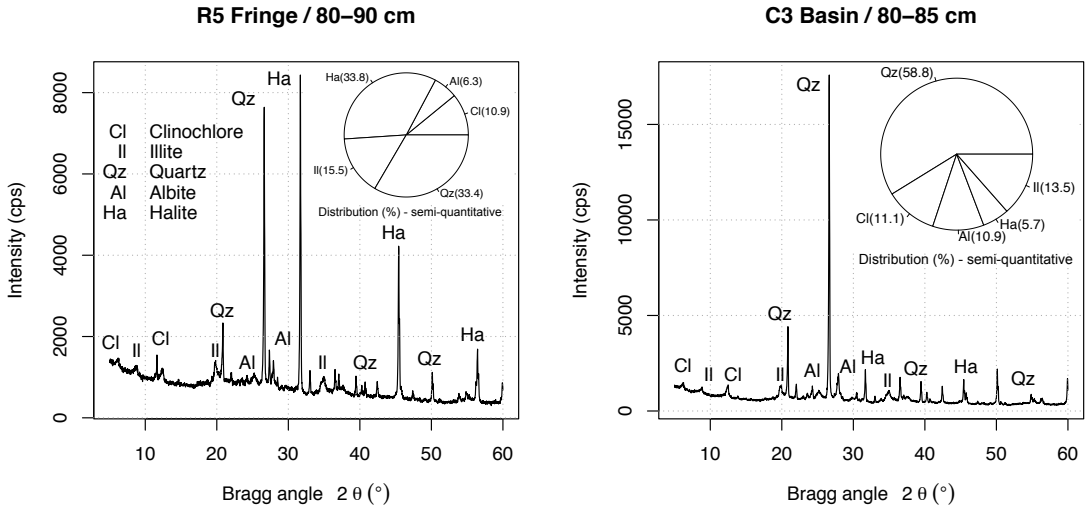


*Figure 23: XRD patterns ($\lambda$ = 1.5406 Å) of plot R5 and C3 including semi-quantitative distribution of detected minerals*

As mentioned in subsection 2.6 the more precise analysis of the clay mineral fraction required a special preparation. As shown further in appendix G, all measured ceramic panels exhibit similar XRD patterns. Owing to this, the following explanations are conducted on one representative sample, which is shown in Figures 24 and 25. The first general measurement of the untreated ceramic panels was conducted in a $2\theta$ angle range between 3 and 70° and the measurements after steaming and heating between 3 and 30°. The overall analysis identified the mineral phases clinochlore, illite, quartz and albite using PDF data. Peaks for corundum are related to the ceramic panel surface composition. The semi-quantitative distribution of the clay size fraction shows major proportions for clinochlore and quartz. The XRD measurement combined with Rietveld refinement using Topas (Bruker) for all analysed ceramic panels yielded compositions of 22-25% quartz, 27-31% clinochlore, 30-31% illite, 3-4% albite and 14-18% corundum. These distributions can not be transferred to the whole sample composition, because they refer only to the clay size fraction.

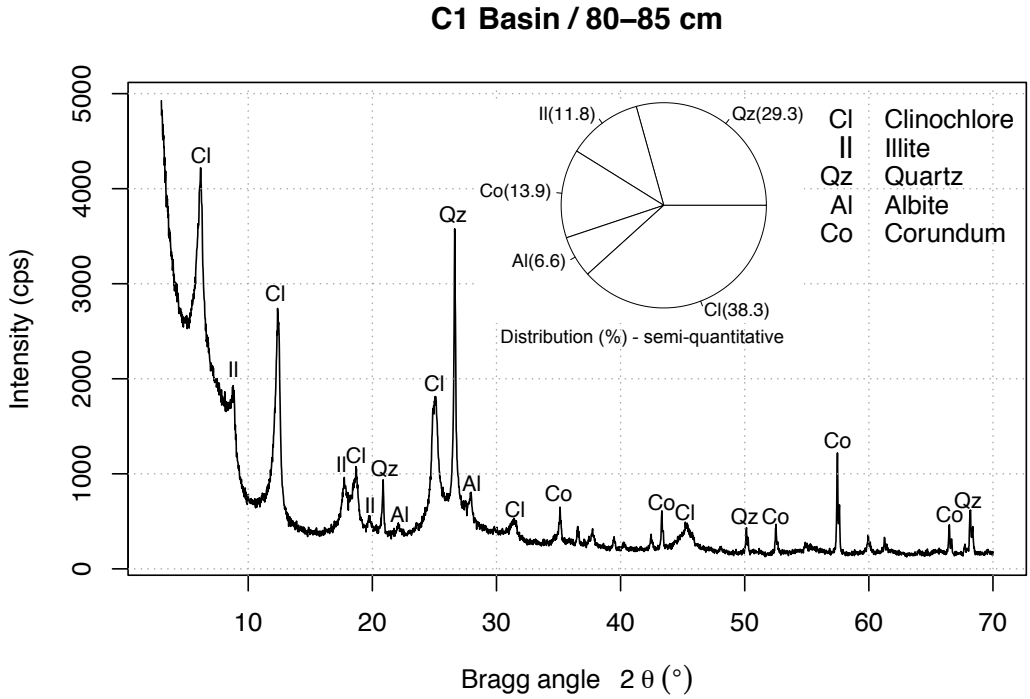


*Figure 24: XRD pattern ($\lambda$ = 1.5406 Å) of extracted clay mineral fraction of basin mangrove sample C1-80-85*

For each measured sample, 3 different XRD patterns were merged for a better clay mineral identification (fig. 25). Glycolation and heating of the ceramic panels implicate swelling or collapsing of the mineral layer structure, what is shown in changed peak distances or rather their complete extinction. Illite is distinguished by the (00l) series 10Å, 5Å, 3.33Å. It is unaffected by glycolation (due to low water holding capacity) and heat treatment (550°C) and therefore the easiest to identify. Apparently illite is a clay mineral which is not easily affected by chemical and heat treatments. For example, it is less subjected to transformation (Bühmann et al., 1985). That steaming has no swelling effect both on illite and clinochlore is mentioned in previous studies (Mackenzie, 1959; Lugwisha, 2011). However, on heating to 550°C, the peaks for clinochlore collapsed (14Å, 7Å, 5Å). Chlorites generally survive heat treatment (350°C and 550°C), but some chlorites

do not and in particular, the interlayers of iron chlorites collapse (Moore and Reynolds, 1989).

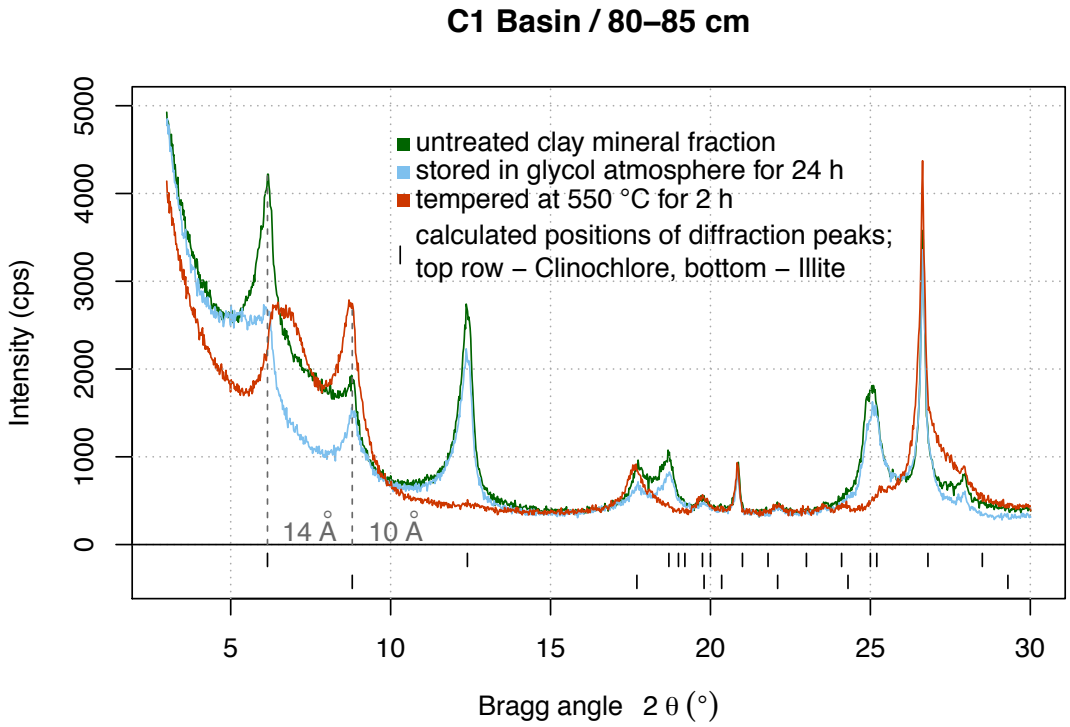


*Figure 25: XRD patterns ($\lambda$ = 1.5406 Å) of different treatments required for the identification of clay minerals in C1-80-85. The ticks below the pattern mark the calculated positions of diffraction peaks of the corresponding clays*

## 3.4 Aluminum-Oxide And Iron-Oxide Contents

Oxalate- and dithionite extraction results show significant differences between basin and fringe mangrove soils ($p$-value <0.001). Basin soils show 2 times higher ppm values of Al ($Al_d$+$Al_o$) than fringe soils and 5 times higher Fe values. In general, metal oxides and hydroxides were more oxalate extractable than dithionite extractable (Fig. 26). While Sinú river samples have similar Al and Fe concentrations to those of basin mangroves in all 4 extraction patterns, metal contents of

sand Nispeyal samples are constantly low. $Fe_o$ contents differ extremely for basin soils, especially for the first 2 depth intervals. Both, basin and fringe soils show an increase of metal oxides within the first depth intervals and in turn a decrease within the deeper levels.

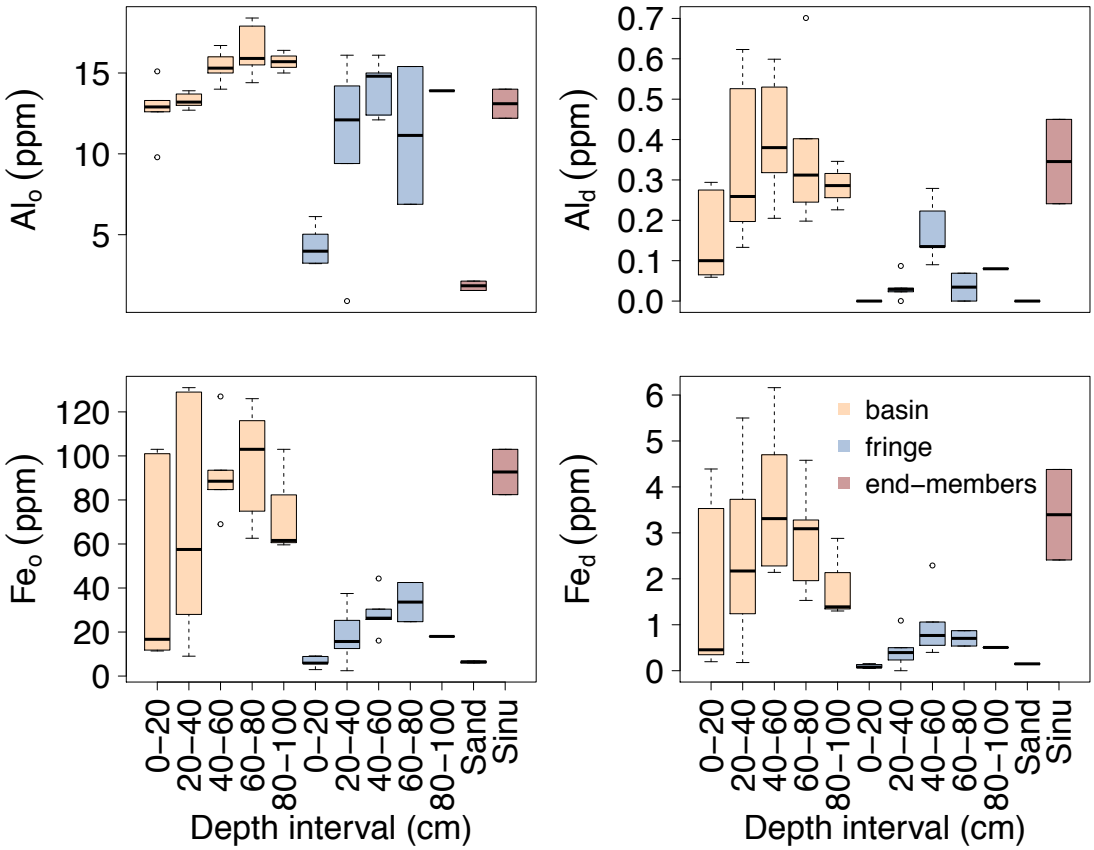


*Figure 26: Oxalate (o)- and dithionite (d) extracted metal oxides for each mangrove type and soil depth (figures in ppm)*

# 4 Interpretation And Discussion

Lower bulk densities in fringe mangrove soils can be explained by their high organic content (e.g. wood residues, leaf debris and roots). Roots claim a large proportion of the soil volume, what clearly decreases its bulk density. Instead,

basin mangrove samples of Cispatá bay are characterised by a dense silty composition including a very small organic part, what results in higher bulk densities. The increase of bulk density with depth in both mangrove types can be interpreted as the result of hydrostatic pressure and time inside the mangrove forest below ground.

Higher OC values in fringe mangrove soils reflect a higher proportion of organic matter and therefore larger organic soil horizons (compare appendix B). Instead, basin mangrove soils are characterised by a larger compressed mineral soil horizon and a small portion of organic topsoil. Because TN concentrations correlate with OC, they show also lower values for basin mangroves, what in turn implies lower decomposition rates of organic matter. The same applies to higher TC/ TN relations for fringe soils. Sand Nispeyal plots show the highest TC/ TN relation, because they have the smallest percentage of TN, but a high percentage of TC (OC + IC). That both end-members (Sinú river and sand Nispeyal samples) contain almost exclusively mineral components is illustrated by their OC contents of nearly 0 %. The assumption, that the marine sediment (sand Nispeyal) samples mainly include carbonates, is confirmed by high IC concentrations only in these plots. As mentioned before, their $CaCO_3$ contents correspond almost exactly to the used carbonate standard (Table E). However, the standard contains only ∼12 % of IC, because C as an element takes only 12 g/mole of 100 g/mole $CaCO_3$.

The decrease of %OC with soil depth is the result of heterotrophic respiration of microorganisms as well as the leaching of dissolved carbon dioxide in water. Because soil microorganisms utilise nitrogen and bacteria fix nitrogen, the concentration of TN also decreases with depth. The point, that concentrations of OC and TN decrease continuously with soil depth, but still show layers with higher concentrations in depths of 80-100 cm (basin) and 60-80 cm (fringe), reflects different sedimentation rates (Bolívar et al., 2015). In Cispatá bay, silting processes

linked to changes in the position of the Sinú river delta, current sea level rise, flooding regime and fluvial inputs, can generate deep organic layers which may cause the increase of OC with depth for both mangrove types.

Higher TOC values in basin mangrove soils reflect higher rates of organic matter accumulation. According to the previous study of Bolívar et al. (2015), the percentage of clay is similar between both mangrove types. However, the silt fraction dominates in all soil profiles in basin mangroves, while sand dominates in fringe mangrove soils. It has been well established that soil particles with greater surface area, as typical of finer textures like those found in basin mangroves, deteriorate drainage conditions which in turn increase retention of organic matter (Bolívar et al., 2015; Prasad and Ramanathan, 2008). Because TOC is linked to %OC, it shows also an increase of TOC in depth levels 80-100 cm (basin) and 60-80 cm (fringe).

The results of the TOC analyses are consistent with hypothesis 1. Therefore, it can be concluded, that basin mangrove soils show a significant higher range of in situ produced carbon than fringe mangrove soils and with it a higher carbon storage of 661±92 MgC/ha (0-100 cm) compared to 320±17 MgC/ha (0-80 cm). Based on the IC concentration results, it is assumed, that marine sediments across Cispatá bay have no influence on additional entered carbon via tidal flooding, because no other plot has a relevant IC content compared to the coral sands of Nispeyal beach. Consequently, hypothesis 2 can be rejected.

$\delta^{13}$C signatures of fringe mangrove sediments are more $^{13}$C depleted than basin sediments. It can therefore be concluded, that they are more plant derived: Plants adsorb more negative $^{13}$C, especially C3 plants are characterised by $^{13}$C values from -22 to -38 ‰ while C4 plants show values between -8 to -15 ‰ (Yeh and Wang, 2001). C3 mangrove species *R. mangle* mostly occurs in the fringe area of Cispatá bay (Bolívar et al., 2015) and is therefore the main producer of $^{13}$C in that

type of forest. In terms of the origin of C this means, that it is produced in situ in that area. Basin mangrove sediments show a higher range of $\delta^{13}$C signatures and more positive values. This could mean either, that the basin area has a stronger influence by C4 grasses, or that the sediments are more mineral derived. Because most common basin mangrove species *A. germinans* is also a C3 plant and there is no influence of C4 grasses, it is assumed that basin mangrove sediments are mostly influenced by entered sediments of the Sinú river. This assumption is confirmed by the fact that basin samples tend to have more enriched $^{13}$C values close to that of Sinú river samples (-25 ‰). According to Ruttenberg and Goni (1997) and Powers and Veldkamp (2005), $\delta^{13}$C signatures of tropical mineral soils range from -23 to -26 ‰, which would underpin mineral derived $^{13}$C values in Cispatá bay. Because $^{13}$C is significant between basin and fringe sediments (see section 3) and because fringe samples only have plant derived $^{13}$C, it can be concluded, that the fringe area is not influenced by the Sinú river delta. It also does not show any influence through marine sediments, because it does not have any enriched signatures comparable to the Nispeyal sand (-5 ‰). Relating to hypothesis 2, the $\delta^{13}$C analyses confirmed, that additional entered carbon is only terrestrial and not marine derived. Moreover, it shows that additionally terrestrial entered carbon only influences basin mangrove sediments while carbon in fringe soils is produced in situ by the plants.

One potential reason for the non-monotonous decline in $^{14}$C with depth (Fig. 19) is the temporal variability in sedimentation rates. Higher OC concentrations in depths of 80-100 cm (basin) and 60-80 cm (fringe) correspond to the enrichment of $^{14}$C in basin and fringe mangroves. Accordingly, these interlayers contain younger carbon compounds than the surrounding soil. Further, the enrichment of $^{14}$C at all post-bomb fringe samples in depths of around 30 cm can be interpreted using the Northern Hemisphere atmospheric $\Delta^{14}CO_2$ model (Fig. 20): After the strong

930 increase of $\Delta^{14}CO_2$ from 1950 to 1965 caused by bomb tests, a continuos depletion of radiocarbon in the atmosphere was recorded in the following decades due to the reduced production of $^{14}C$ and radioactive decay. Because of the relatively rapid cycling of C between the atmosphere and living biomass, most fast-growing tissues of plants growing in pre-industrial times maintained a $^{14}C/^{12}C$ value equal 935 to that of atmospheric $CO_2$ (Schuur et al., 2016). According to the carbon cycle and the decomposition of C in soil, fringe soil samples with depths of 30 cm show an enrichment of $^{14}C$ towards the same plot samples with depths of 10 cm, because the atmosphere was more enriched in $^{14}C$ in 1980 than in 2000 (Fig. 20).

The mineralogical composition of the Sinú river delta sediments of Cispatá bay 940 is similar to the composition of the Sinú river sediments in Montería. It can be therefore concluded, that basin and fringe mangrove sediments were transported by the river and have their distant origin in that river basin. The Sinú river has its origin in the north-western Andes Cordillera, which are overlapped by basaltic volcanic rocks. Quartz and Albite are the major substitutes of that river 945 basin. Clinochlore, which is the Mg-rich substitute of the chlorite group, was formed hydrothermally metamorphic or secondary as a transformation product of mica, garnet, pyroxene or amphibole. Illite was probably formed by river water - sediment interactions. More precisely, it was formed by hydration of mica and partially compensation of $K^+$ by $H_3O^+$. Next to the other plots, especially plot 950 R5 shows intense peaks for halite in depths between 80-90 cm. Halite crystallises by the evaporation of sea water and intense salinisation occurring in the mangrove habitat. Its occurrence verifies that the fringe mangrove area has tidal influence of hyper saline sea water, but probably not of marine sediments (as mentioned before). Furthermore, halite confirms the sediment air exposition, since it needs 955 evaporation to be formed. That halite reaches that intense proportion in depths of 80-90 cm can be attributed to the changing course of the Sinú river. From 1849

-1938 (Suarez, 2004), the river course passed the northern main land of Cispatá bay, where R5 is located. Accordingly, the sedimentation rate increased in that period. However, before that period, this region was more influenced by saline sea water, what results in intense halite peaks. That basin soils also contain halite, shows that they are also flooded occasionally. Sand Nispeyal samples mostly contain carbonates, which were formed out of marine water. Because sea water contains magnesium, which favours the formation of aragonite towards calcite, shells and corals of the Nispeyal sand primarily consist of aragonite. The sand samples also contain a low proportion of quartz, which is presumably entered via the delta of the Sinú river.

Depending on their cation-exchange capacity, clay minerals are able to bind metal oxides. Because cation-exchange sites on clay and humic colloids have negative charge, cations (metals) from the soil solution must satisfy this charge, so that mineral and organic surfaces appear to be charged neutral. Cations are retained on these clay sites by electrostatic forces. At the same time, Al and Fe oxide interactions with clays are pH dependent (variable charges). At low pH, where the oxides carry sufficient positive charge, they precipitate on clay surfaces. These coatings, once formed, are stable at higher pHs. Precipitation of oxides at high pH occurs as phases separated from the clays (Goldberg, 1989). According to Goldberg (1989), observed precipitation of oxides showed, that only amorphous Fe-precipitates were obtained with the clay substrate. However, in the case of quartz, precipitated oxides had increased crystallinity, particularly for the samples with high iron concentrations. Transferred to the studied area of Cispatá bay, this explains that the increased proportion of metal oxides in basin soils goes together with a more mineralogical composed soil in that area.

As explained by $^{13}C$ signatures, basin mangrove sediments are terrestrially derived. This finding is also reflected in higher metal oxide and hydroxide contents

compared to fringe mangrove soils, with ppm contents similar to those of the Sinú river samples (Fig. 26). Because basin mangroves have much older and more compact sediments with a greater proportion of mineral layers, the alteration of minerals and the formation of metal oxides, hydroxides and clay minerals is supported in their soils. The contents of metal oxides in Cispatá bay are generally low, compared to other soil studies (McKeague and Day, 1966). Also, mangrove soils in Cispatá bay do not show typical reddish colour changes, which are an indication for iron oxides, especially for hematite. A continuous grey colouring of all non-humus layers shows further the only presence of clay minerals (Ségalen, 1971). Only plot C1 contains yellow and beige coloured layers in depths of 40-80 cm (appendix B), what indicates the occurrence of goethite ($\alpha$-$Fe^{3+}O(OH)$). Beside goethite, also gibbsite ($Al(OH)_3$), indicated by a white colour, is a typical hydroxide for mangrove sediments (Souza-Júnior et al., 2008) and soils of warm and humid areas of the world (Ségalen, 1971). As mentioned in section 3, Al and Fe were more oxalate- than dithionite extractable. This leads to the conclusion that Al and Fe oxides and hydroxides are mostly present as amorphous products, e.g. as alumo- or ferrogels. The negligible small amounts of metal oxides and hydroxides in sand samples indicate furthermore, that those transported as well as in situ produced oxides get fixed in mangrove soils. An increase of Al and Fe is apparent within the first depth intervals, but there is no continuos trend with depth. Again, this shows the connection between mineral soil horizons and Al and Fe bonding and the smaller amount of Al and Fe in humus layers.

That mineral surfaces of Al and Fe oxides and hydroxides adsorb dissolved organic matter (DOM) has been well established (Kaiser and Guggenberger, 2000; Tipping, 1981). It is therefore very likely, that metal oxides and hydroxides bind and preserve C in basin mangrove soils. According to Kaiser and Guggenberger (2000), the capacity to adsorb DOM relates to the presence of Al and Fe oxides

and hydroxides. The sorption of DOM derived from decomposition to Al and Fe oxyhydroxides involves strong complexation bondings between surface metals and acidic organic ligands, particularly with those associated with aromatic structures. The strength of the sorption relates further to the surface properties of the sorbing mineral phase. Kaiser and Guggenberger (2000) found out, that dissolved organic matter sorption is strongly enhanced by hydrous oxide coatings and particularly by amorphous $Al(OH)_3$, what underpins that amorphous hydroxides bind C in basin soils of Cispatá bay. Tipping (1981) describes moreover, that the extent of adsorption of DOM increases with decreasing pH. Because mangrove soils at the Colombian Caribbean coast have an acid character both at *A. germinans* and *R. mangle* forests (Urrego et al., 2014), a stronger C binding onto oxides and hydroxides is substantiated in that region. These results are consistent with hypothesis 3.

# 5 Conclusion

In summary and in clarification of the question, where do the unusually high carbon concentrations in basin soils of Cispatá bay have there origin? I can conclude: On the one hand, carbon is produced in situ both in fringe and basin mangroves and it is bound to the mineral fraction, especially in basin soils. The basin structure in that type of forest slows furthermore the drainage of dissolved carbon into the ocean. $\delta^{13}$C and $\Delta^{14}$C signatures return the result, that sediments of the delta have a terrestrial origin. Carbon adsorbed on surfaces of metal oxides, which in turn are precipitated on quartz and clay mineral surfaces, enters additionally the studied area via the Sinú river delta and leads to increased carbon values.

That mangrove soils of Cispatá bay show those high differences referred to their carbon stock compared to other mangrove forests on earth (section 1.1) is therewith based on their constantly terrestrial carbon input through the Sinú river and also on the basin structure of the further inland mangrove area. It might be of interest, to start another study, where different mangrove forests across the earth are compared with regard to the influence of their countryside structure, their estuaries, mangroves species and their carbon source, to find out if there are regions with similar causes for high carbon contents.

# References


Alfaro, E. and Holz, M. (2014). Stratigraphic relationships between the Colombian, Sinú Offshore and Sinú-San Jacinto basins based on seismic stratigraphy. *Brazilian Journal of Geology*, 44(4):607–625.

Alongi, D. (2009). *The Energetics of Mangrove Forests*. Springer Science & Business Media.

Bolívar, J., Urrego, L., Moreno, F., Mira, J., Herrera, D., and Posada, J. (2015). Soil And Root Carbon In Two Types Of Mangroves In Cispatá Bay (Colombian Caribbean). Master's thesis, Corporación Centro de Investigación en Ecosistemas y Cambio Global Carbono y Bosques.

Bühmann, C., Fey, M., and De Villiers, J. (1985). Aspects of the X-ray identification of swelling clay minerals in soils and sediments. *South African journal of science*, 81(8):505–509.

Castaño, A., Urrego, L., and Bernal, G. (2010). Mangrove dynamics in the Cispata lagoon system (Colombian Caribbean) during last 900 years. *Revista de biologia tropical*, 58(4):1347–1366.

Duke, N. C., Meynecke, J.-O., Dittmann, S., Ellison, A. M., Anger, K., Berger, U., Cannicci, S., Diele, K., Ewel, K. C., Field, C. D., et al. (2007). A World Without Mangroves? *Science*, 317(5834):41–42.

Elmqvist, T. and Cox, P. A. (1996). The evolution of vivipary in flowering plants. *Oikos*, pages 3–9.

Feller, I. and Sitnik, M. (1996). Mangrove ecology: A Manual For A Field Course. A Field Manual Focused On The Biocomplexity On Mangrove Ecosystems. *Smithsonian Institution, Washington*.

Flinch, J. (2003). Structural evolution of the Sinu-Lower Magdalena area (northern Colombia). *AAPG Special Volumes*.

Giri, C., Ochieng, E., Tieszen, L. L., Zhu, Z., Singh, A., Loveland, T., Masek, J., and Duke, N. (2011). Status and distribution of mangrove forests of the world using earth observation satellite data. *Global Ecology and Biogeography*, 20(1):154–159.

Goldberg, S. (1989). Interaction of aluminum and iron oxides and clay minerals and their effect on soil physical properties: a review. *Communications in soil science and plant analysis*, 20(11-12):1181–1207.

Gu, B., Schmitt, J., Chen, Z., Liang, L., and McCarthy, J. F. (1995). Adsorption and desorption of different organic matter fractions on iron oxide. *Geochimica et Cosmochimica Acta*, 59(2):219–229.

Hilke, I. (2016). Analytical Principle. https://www.bgc-jena.mpg.de/service/chem_lab/roma/index.php/Labor/Elemental_Analysis.

Hoffmann, G. (1991). *Verband Deutscher Landwirtschaftlicher Untersuchungs-und Forschungsanstalten. Methodenbuch. Band I. Die Untersuchung von Böden.* VDLUFA-Verlag Darmstadt, Germany.

Jasmund, K. and Lagaly, G. (1993). Tonminerale und Tone. *Darmstadt: Steinkopff-Verlag*.

Kaiser, K. and Guggenberger, G. (2000). The role of DOM sorption to mineral surfaces in the preservation of organic matter in soils. *Organic geochemistry*, 31(7):711–725.

Kellogg, J., Toto, E., and Cerón, J. (2005). Structure and tectonics of the Sinu-San Jacinto accretionary prism in northern Colombia. In *X Congreso Colombiano de Geologia*, pages 1–10.

Khan, M. N. I., Suwa, R., and Hagihara, A. (2007). Carbon and nitrogen pools in a mangrove stand of Kandelia obovata (S., L.) Yong: vertical distribution in the soil-vegetation system. *Wetlands Ecology and Management*, 15(2):141–153.

Lambeth, D. O. and Palmer, G. (1973). The kinetics and mechanism of reduction of electron transfer proteins and other compounds of biological interest by dithionite. *Journal of Biological Chemistry*, 248(17):6095–6103.

Lewis, R., Brown, B., Quarto, A., Enright, J., Corets, E., Primavera, J., Ravishankar, T., Stanley, O., and Djamaluddin, R. (2006). Five steps to successful ecological restoration of mangroves. *Mangrove Action Project/Yayasan Akar Rumput Laut, Yogyakarta*.

Lugo, A. E. and Snedaker, S. C. (1974). The Ecology Of Mangroves. *Annual review of ecology and systematics*, pages 39–64.

Lugwisha, E. (2011). Identification of Clay Minerals of the Eastern Southern Region of Lake Victoria by Ethylene Glycol and Heat: Xray Diffraction and Infrared Spectroscopy Studies. *Tanzania Journal of Science*, 37(1).

Mackenzie, R. (1959). The classification and nomenclature of clay minerals. *Clay Min. Bull*, 4:52–66.

McKeague, J. and Day, J. (1966). Dithionite-and oxalate-extractable Fe and Al as aids in differentiating various classes of soils. *Canadian journal of soil science*, 46(1):13–22.

Middelburg, J. J. and Herman, P. M. (2007). Organic matter processing in tidal estuaries. *Marine Chemistry*, 106(1):127–147.

Moore, D. M. and Reynolds, R. C. (1989). *X-ray Diffraction and the Identification and Analysis of Clay Minerals*, volume 378. Oxford university press Oxford.

Muccio, Z. and Jackson, G. P. (2009). Isotope ratio mass spectrometry. *Analyst*, 134(2):213–222.

National Oceanic and Atmospheric Administration (2014). NOAA Assisting UN Spill Response Team in Bangladesh.

Powers, J. S. and Veldkamp, E. (2005). Regional variation in soil carbon and $\delta$13C in forests and pastures of northeastern Costa Rica. *Biogeochemistry*, 72(3):315–336.

Prasad, M. B. K. and Ramanathan, A. (2008). Sedimentary nutrient dynamics in a tropical estuarine mangrove ecosystem. *Estuarine, Coastal and Shelf Science*, 80(1):60–66.

Raessler, M. (2016). Wissenschaftlicher Servicebereich - Labor für Spektrometrie.

Ramsey, C. B., Dee, M., Lee, S., Nakagawa, T., and Staff, R. A. (2010). Developments in the calibration and modeling of radiocarbon dates. *Radiocarbon*, 52(3):953–961.

Reimer, P. J., Baillie, M. G., Bard, E., Bayliss, A., Beck, J. W., Bertrand, C. J., Blackwell, P. G., Buck, C. E., Burr, G. S., Cutler, K. B., et al. (2004). IntCal04 terrestrial radiocarbon age calibration, 0–26 cal kyr BP. *Radiocarbon*.

Ruttenberg, K. and Goni, M. (1997). Phosphorus distribution, C: N: P ratios, and $\delta$ 13 C oc in arctic, temperate, and tropical coastal sediments: tools for characterizing bulk sedimentary organic matter. *Marine Geology*, 139(1):123–145.

Schuur, E. A., Druffel, E. R., and Trumbore, S. E. (2016). *Radiocarbon and Climate Change*. Springer.

Ségalen, P. (1971). Metallic oxides and hydroxides in soils of the warm and humid areas of the world: formation, identification, evolution. *Soils and Tropical Weathering. UNESCO, Paris*.

Souza-Júnior, V. S. d., Vidal-Torrado, P., Garcia-Gonzaléz, M. T., Otero, X. L., and Macías, F. (2008). Soil mineralogy of mangrove forests from the state of São Paulo, southeastern Brazil. *Soil Science Society of America Journal*, 72(3):848–857.

Sparks, D. L., Page, A., Helmke, P., Loeppert, R., Soltanpour, P., Tabatabai, M., Johnston, C., Sumner, M., et al. (1996). *Methods of soil analysis. Part 3-Chemical methods.* Soil Science Society of America Inc.

Spieß, L., Teichert, G., Schwarzer, R., Behnken, H., and Genzel, C. (2009). *Moderne Röntgenbeugung: Röntgendiffraktometrie für Materialwissenschaftler, Physiker und Chemiker*. Springer-Verlag.

Spohn, M., Babka, B., and Giani, L. (2013). Changes in soil organic matter quality during sea-influenced marsh soil development at the North Sea coast. *Catena*, 107:110–117.

Spohn, M. and Giani, L. (2012). Carbohydrates, carbon and nitrogen in soils of a marine and a brackish marsh as influenced by inundation frequency. *Estuarine, Coastal and Shelf Science*, 107:89–96.

Suarez, B. E. S. (2004). The Sinú river delta on the northwestern Caribbean coast of Colombia: bay infilling associated with delta development. *Journal of South American Earth Sciences*, 16(7):623–631.

Tamooh, F., Huxham, M., Karachi, M., Mencuccini, M., Kairo, J., and Kirui, B. (2008). Below-ground root yield and distribution in natural and replanted mangrove forests at Gazi bay, Kenya. *Forest Ecology and Management*, 256(6):1290–1297.

Thibodeau, F. R. and Nickerson, N. H. (1986). Differential oxidation of mangrove substrate by Avicennia germinans and Rhizophora mangle. *American Journal of Botany*, pages 512–516.

Tipping, E. (1981). The adsorption of aquatic humic substances by iron oxides. *Geochimica et Cosmochimica Acta*, 45(2):191–199.

Tomlinson, P. (1986). The Botany Of Mangroves. Cambridge Tropical Biology Series.

Urrego, L., Molina, E., and Suárez, J. (2014). Environmental and anthropogenic influences on the distribution, structure, and floristic composition of mangrove forests of the Gulf of Urabá (Colombian Caribbean). *Aquatic Botany*, 114:42–49.

Werner, R. A. and Brand, W. A. (2001). Referencing strategies and techniques in stable isotope ratio analysis. *Rapid Communications in Mass Spectrometry*, 15(7):501–519.

Yeh, H.-W. and Wang, W.-M. (2001). Factors affecting the isotopic composition of organic matter.(1) Carbon isotopic composition of terrestrial plant materials. *Proceedings of the National Science Council, Republic of China. Part B, Life sciences*, 25(3):137–147.

# Appendix

## A - List Of Soil Samples With Each Depth And Mangrove Type

| Plot Number | Depth [cm] | Type |
|---|---|---|
| P21 | 0-20 | Fringe |
| P21 | 21-40 | Fringe |
| P21 | 41-60 | Fringe |
| P21 | 61-80 | Fringe |
| P21 Bulk density | 0-20 | Fringe |
| P21 Bulk density | 21-40 | Fringe |
| P21 Bulk density | 41-60 | Fringe |
| P21 Bulk density | 61-80 | Fringe |
| R1 | 0-15 | Fringe |
| R1 | 16-25 | Fringe |
| R1 | 26-35 | Fringe |
| R1 | 36-57 | Fringe |
| R1-Replication | 0-15 | Fringe |
| R1-Replication | 16-30 | Fringe |
| R1-Replication | 31-40 | Fringe |
| R1-Replication | 41-57 | Fringe |
| R4 | 0-20 | Fringe |
| R4 | 21-40 | Fringe |
| R5 | 0-20 | Fringe |
| R5 | 21-40 | Fringe |
| R5 | 41-50 | Fringe |
| R5 | 51-60 | Fringe |
| R5 | 61-80 | Fringe |
| R5 | 81-90 | Fringe |
| R6 | 0-20 | Fringe |
| R6 | 21-27 | Fringe |
| R6 | 28-45 | Fringe |
| R6-Replication | 0-20 | Fringe |
| R6-Replication | 21-40 | Fringe |
| R6-Replication | 41-47 | Fringe |
| R6-Replication | 48-54 | Fringe |

| Plot Number | Depth [cm] | Type |
|---|---|---|
| P16 | 0-20 | Basin |
| P16 | 21-30 | Basin |
| P16 | 31-50 | Basin |
| P16 | 51-65 | Basin |
| P16 | 66-85 | Basin |
| P16 | 86-95 | Basin |
| C1 | 0-20 | Basin |
| C1 | 21-40 | Basin |
| C1 | 41-60 | Basin |
| C1 | 61-80 | Basin |
| C1 | 81-85 | Basin |
| C2 | 0-20 | Basin |
| C2 | 21-40 | Basin |
| C2 | 41-60 | Basin |
| C2 | 61-70 | Basin |
| C3 | 0-20 | Basin |
| C3 | 21-40 | Basin |
| C3 | 41-60 | Basin |
| C3 | 61-80 | Basin |
| C3 | 81-85 | Basin |
| C4 | 0-20 | Basin |
| C4 | 21-40 | Basin |
| C4 | 41-60 | Basin |
| C4 | 61-77 | Basin |
| C4 Replication | 0-10 | Basin |
| C4 Replication | 11-20 | Basin |
| C4 Replication | 21-30 | Basin |
| C4 Replication | 31-36 | Basin |
| C4 Replication | 37-47 | Basin |
| C4 Replication | 48-57 | Basin |
| C4 Replication | 58-64 | Basin |
| C4 Replication | 65-74 | Basin |
| C4 Replication | 75-84 | Basin |
| C4 Bulk density | 0-20 | Basin |
| C4 Bulk density | 21-40 | Basin |
| C4 Bulk density | 41-60 | Basin |
| C4 Bulk density | 61-80 | Basin |
| C4 Bulk density | 81-100 | Basin |
| Sinú River | 0-100 | / |
| Sand Nispeyal | 0-100 | / |

# B - Soil Profiles

## P21-Fringe

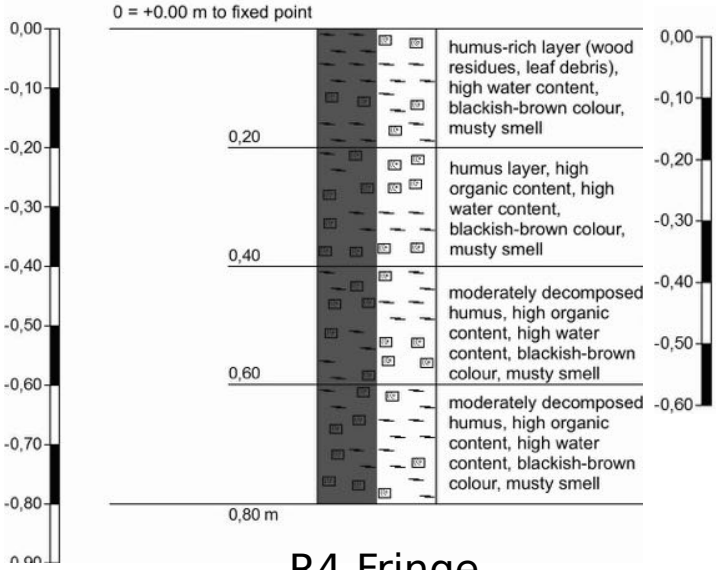


## R1-Fringe

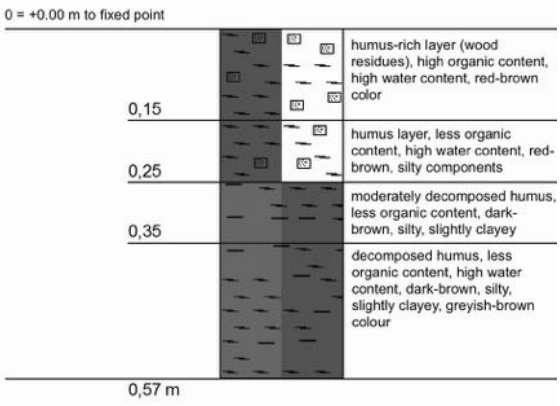


## R4-Fringe

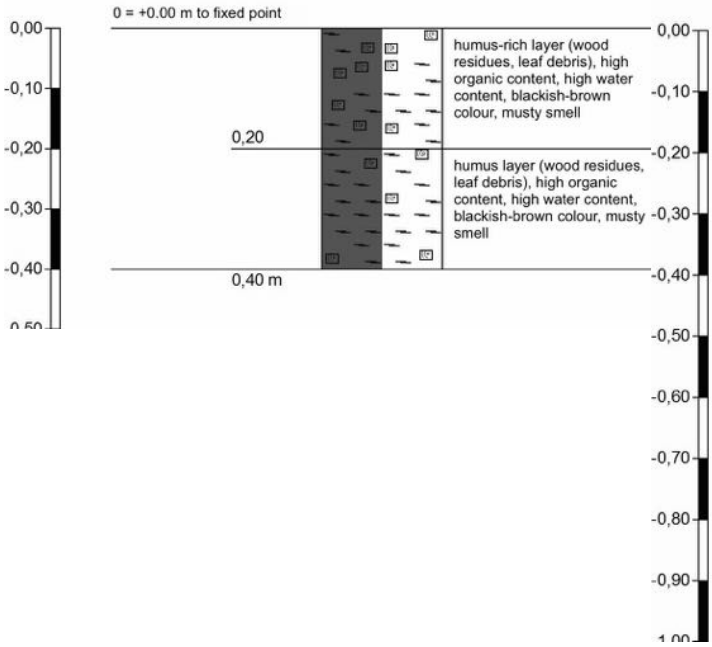


## R5-Fringe

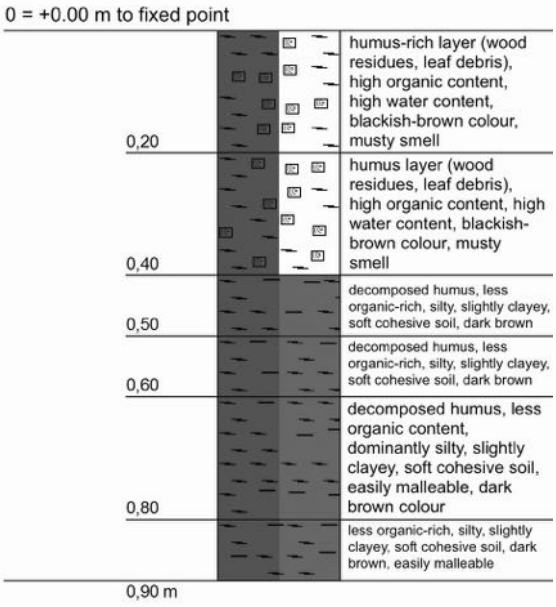

## R6-Fringe

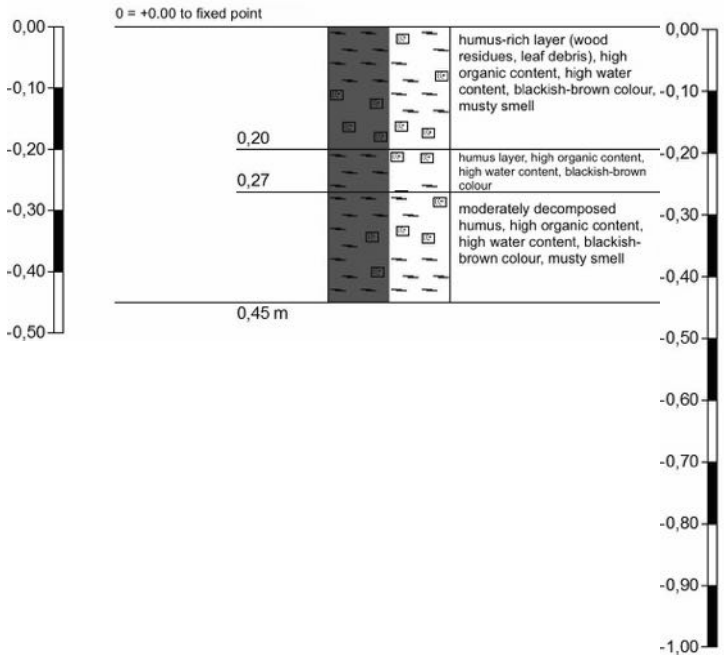


## P16-Basin

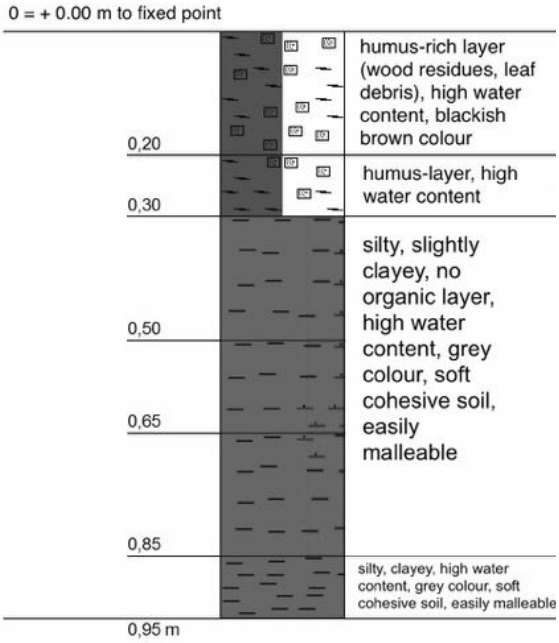


## C1-Basin

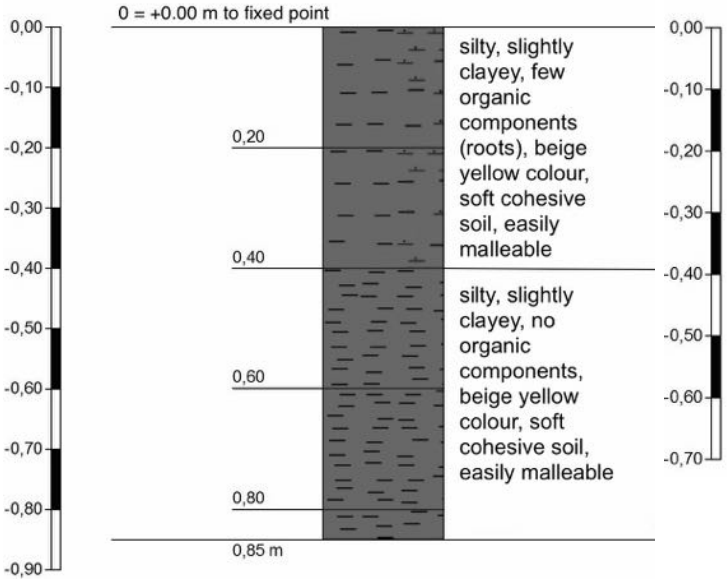


## C2-Basin

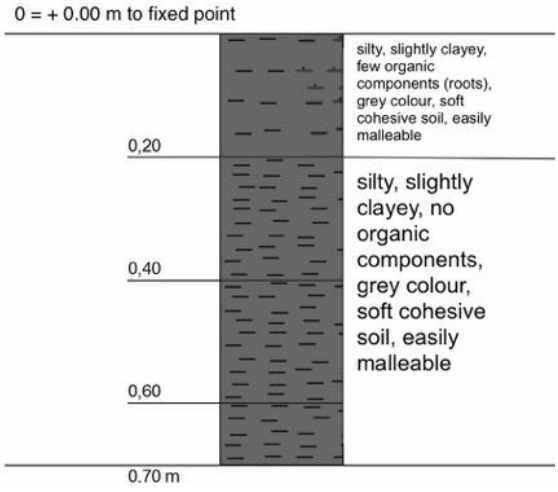

## C3-Basin

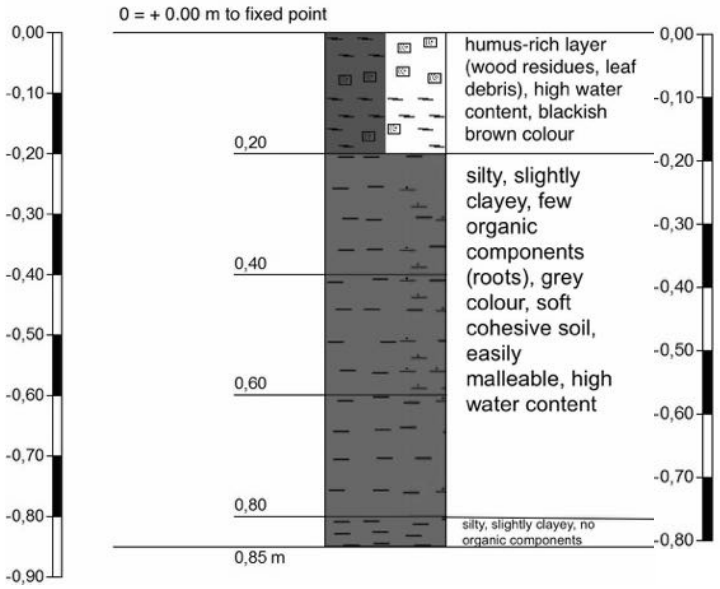


## C4-Basin

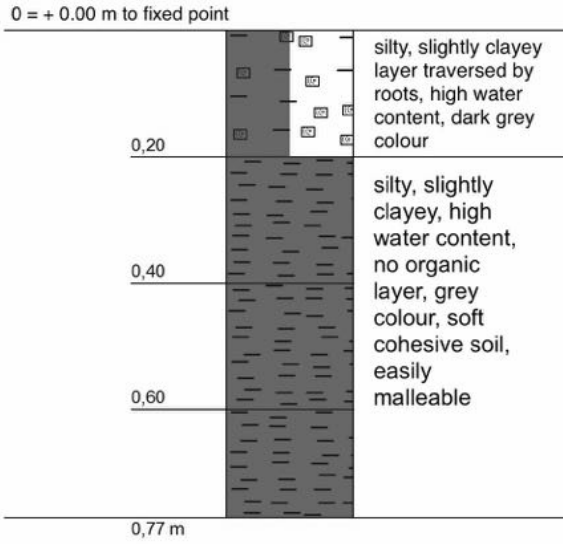


## End-member: Sand Nispeyal

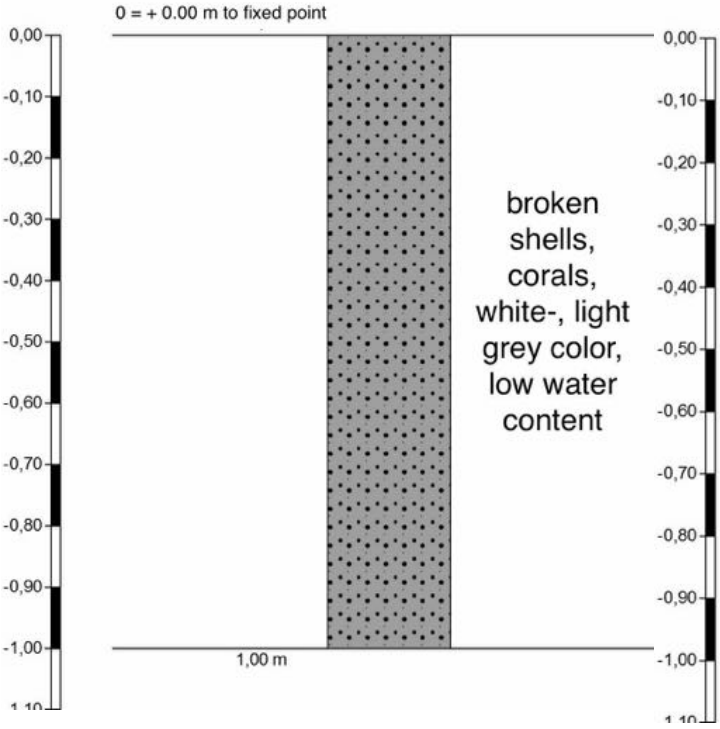


## End-member: Sinu River

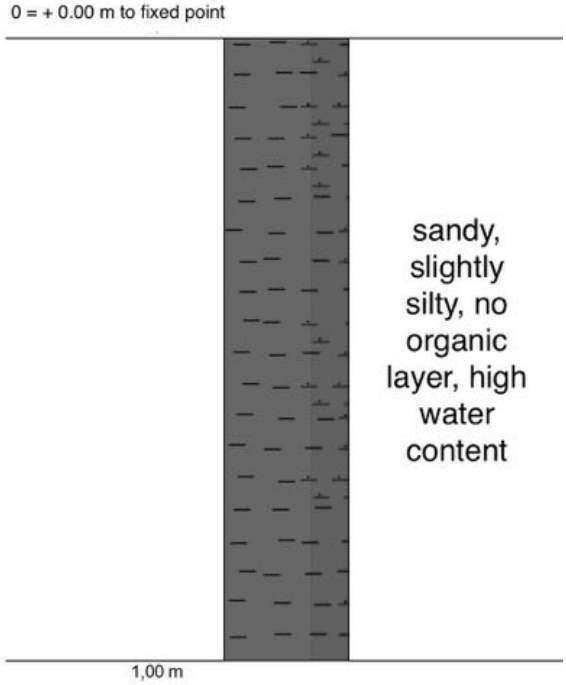

# C - Water Loss Recording Of Bulk Density Samples Dried At 105°C

| Plot Number | Depth [cm] | Weight [g] 11.04.16 | Weight [g] 12.04.16 | Weight [g] 13.04.16 | Weight [g] 14.04.16 |
|---|---|---|---|---|---|
| P21 | 0-20 | 28.93 | 28.79 | 28.62 | 28.62 |
| P21 | 0-20 | 27.13 | 27.07 | 27.02 | 26.79 |
| P21 | 0-20 | 26.29 | 26.29 | 26.18 | 26.09 |
| P21 | 21-40 | 24.06 | 23.97 | 23.91 | 23.84 |
| P21 | 21-40 | 26.88 | 26.57 | 26.47 | 26.34 |
| P21 | 21-40 | 22.98 | 22.75 | 22.68 | 22.64 |
| P21 | 41-60 | 33.25 | 33.09 | 32.92 | 32.82 |
| P21 | 41-60 | 24.55 | 24.46 | 24.40 | 24.38 |
| P21 | 41-60 | 25.50 | 24.84 | 24.74 | 24.71 |
| P21 | 61-80 | 29.76 | 29.41 | 29.07 | 29.07 |
| P21 | 61-80 | 30.24 | 29.72 | 29.55 | 29.45 |
| P21 | 61-80 | 29.90 | 29.44 | 29.41 | 29.25 |
| C4 | 0-20 | 109.65 | 108.30 | 107.80 | 107.62 |
| C4 | 0-20 | 110.21 | 108.81 | 108.41 | 108.09 |
| C4 | 0-20 | 120.25 | 119.62 | 119.31 | 118.84 |
| C4 | 21-40 | 137.01 | 135.99 | 135.52 | 135.19 |
| C4 | 21-40 | 144.88 | 144.64 | 144.40 | 144.12 |
| C4 | 21-40 | 127.02 | 126.60 | 126.36 | 126.03 |
| C4 | 41-60 | 129.23 | 128.86 | 128.65 | 128.47 |
| C4 | 41-60 | 96.47 | 96.04 | 95.83 | 95.60 |
| C4 | 41-60 | 127.98 | 127.71 | 127.50 | 127.25 |
| C4 | 61-80 | 128.94 | 128.62 | 128.32 | 128.02 |
| C4 | 61-80 | 132.06 | 131.58 | 131.07 | 130.93 |
| C4 | 61-80 | 103.25 | 102.58 | 102.58 | 102.41 |
| C4 | 81-100 | 104.97 | 104.42 | 103.98 | 103.63 |
| C4 | 81-100 | 89.32 | 88.87 | 88.72 | 88.52 |
| C4 | 81-100 | 93.94 | 93.49 | 93.15 | 92.87 |

| Plot Number | Depth [cm] | Weight [g] 15.04.16 | Weight [g] 19.04.16 | Weight [g] 21.04.16 | Weight [g] 26.04.16 | Final Weight [g] 27.04.16 |
|---|---|---|---|---|---|---|
| P21 | 0-20 | 17.78 | 16.88 | 16.81 | 16.79 | 16.77 |
| P21 | 0-20 | 16.06 | 15.29 | 15.20 | 15.20 | 15.19 |
| P21 | 0-20 | 15.36 | 14.56 | 14.47 | 14.47 | 14.46 |
| P21 | 21-40 | 13.06 | 12.43 | 12.35 | 12.33 | 12.32 |
| P21 | 21-40 | 15.41 | 14.58 | 14.51 | 14.51 | 14.51 |
| P21 | 21-40 | 11.65 | 11.08 | 10.95 | 10.92 | 10.91 |
| P21 | 41-60 | 21.93 | 21.16 | 21.04 | 21.02 | 21.02 |
| P21 | 41-60 | 13.63 | 13.01 | 12.92 | 12.92 | 12.90 |
| P21 | 41-60 | 13.85 | 13.22 | 13.13 | 13.10 | 13.10 |
| P21 | 61-80 | 18.10 | 17.29 | 17.20 | 17.17 | 17.15 |
| P21 | 61-80 | 18.69 | 17.95 | 17.85 | 17.84 | 17.81 |
| P21 | 61-80 | 18.32 | 17.50 | 17.41 | 17.40 | 17.36 |
| C4 | 0-20 | 96.68 | 95.63 | 95.55 | 95.55 | 95.54 |
| C4 | 0-20 | 97.15 | 95.87 | 95.81 | 95.81 | 95.79 |
| C4 | 0-20 | 107.60 | 106.26 | 106.23 | 106.23 | 106.22 |
| C4 | 21-40 | 124.24 | 123.07 | 122.98 | 122.98 | 122.98 |
| C4 | 21-40 | 133.11 | 131.95 | 131.88 | 131.88 | 131.88 |
| C4 | 21-40 | 114.56 | 113.24 | 113.16 | 113.16 | 113.16 |
| C4 | 41-60 | 117.41 | 116.33 | 116.26 | 116.26 | 116.25 |
| C4 | 41-60 | 84.14 | 83.01 | 82.95 | 82.94 | 82.94 |
| C4 | 41-60 | 116.16 | 115.12 | 115.05 | 115.05 | 115.05 |
| C4 | 61-80 | 116.71 | 115.61 | 115.52 | 115.52 | 115.52 |
| C4 | 61-80 | 119.90 | 118.62 | 118.56 | 118.56 | 118.56 |
| C4 | 61-80 | 91.07 | 89.95 | 89.91 | 89.91 | 89.91 |
| C4 | 81-100 | 92.44 | 91.14 | 91.06 | 90.96 | 90.96 |
| C4 | 81-100 | 78.75 | 76.48 | 76.45 | 76.40 | 76.39 |
| C4 | 81-100 | 81.76 | 80.59 | 80.53 | 80.51 | 80.49 |

# D - Weighing Process For The Determination Of Dry Matter

| Plot Number | Depth [cm] | Empty Glass [g] | Sample Weigh-In (∼3g) | Sample Weight + Glass [g] | Sample Weight [g] after Drying | Dry Matter Content [%] |
|---|---|---|---|---|---|---|
| P21 | 0-20 | 13.37 | 3.09 | 16.26 | 2.88 | 93.50 |
| P21 | 21-40 | 13.55 | 3.14 | 16.48 | 2.93 | 93.30 |
| P21 | 41-60 | 13.36 | 3.11 | 16.25 | 2.89 | 92.86 |
| P21 | 61-80 | 14.06 | 3.02 | 16.92 | 2.86 | 94.60 |
| R1 | 0-15 | 13.40 | 3.04 | 16.25 | 2.85 | 93.87 |
| R1 | 16-25 | 15.94 | 3.03 | 18.82 | 2.88 | 94.94 |
| R1 | 26-35 | 13.17 | 3.11 | 16.18 | 3.01 | 96.76 |
| R1 | 36-57 | 13.17 | 3.06 | 16.12 | 2.96 | 96.72 |
| R1-Replication | 0-15 | 13.11 | 3.02 | 15.94 | 2.84 | 93.97 |
| R1-Replication | 16-30 | 15.73 | 3.15 | 18.72 | 2.99 | 95.09 |
| R1-Replication | 31-40 | 13.17 | 3.12 | 16.20 | 3.03 | 97.02 |
| R1-Replication | 41-57 | 15.88 | 3.13 | 18.96 | 3.08 | 98.16 |
| R4 | 0-20 | 13.54 | 3.08 | 16.42 | 2.88 | 93.58 |
| R4 | 21-40 | 13.47 | 3.06 | 16.32 | 2.85 | 92.95 |
| R5 | 0-20 | 13.61 | 3.12 | 16.52 | 2.90 | 93.09 |
| R5 | 21-40 | 13.86 | 3.08 | 16.74 | 2.87 | 93.21 |
| R5 | 41-50 | 13.62 | 3.14 | 16.62 | 2.99 | 95.29 |
| R5 | 51-60 | 13.56 | 3.09 | 16.46 | 2.90 | 93.73 |
| R5 | 61-80 | 13.40 | 3.03 | 15.87 | 2.47 | 81.64 |
| R5 | 81-90 | 12.97 | 3.04 | 15.86 | 2.90 | 95.13 |
| R6 | 0-20 | 13.33 | 3.04 | 16.16 | 2.83 | 92.94 |
| R6 | 21-27 | 13.28 | 3.04 | 16.14 | 2.86 | 94.05 |
| R6 | 28-45 | 12.66 | 3.03 | 15.52 | 2.86 | 94.38 |
| R6-Replication | 0-20 | 12.98 | 3.07 | 15.87 | 2.89 | 94.05 |
| R6-Replication | 21-40 | 13.51 | 3.12 | 16.45 | 2.94 | 94.27 |
| R6-Replication | 41-47 | 13.63 | 3.17 | 16.67 | 3.04 | 95.69 |
| R6-Replication | 48-54 | 13.29 | 3.08 | 16.26 | 2.97 | 96.26 |
| P16 | 0-20 | 15.46 | 3.08 | 18.37 | 2.92 | 94.76 |
| P16 | 21-30 | 13.19 | 3.07 | 16.11 | 2.92 | 94.91 |
| P16 | 31-50 | 13.21 | 3.09 | 16.05 | 2.84 | 92.00 |
| P16 | 51-65 | 13.07 | 3.09 | 16.10 | 3.03 | 98.12 |
| P16 | 66-85 | 14.40 | 3.18 | 17.28 | 2.88 | 90.79 |
| P16 | 86-95 | 13.21 | 3.07 | 16.24 | 3.03 | 98.62 |
| C1 | 0-20 | 13.64 | 3.12 | 16.70 | 3.05 | 97.93 |
| C1 | 21-40 | 13.77 | 3.08 | 16.79 | 3.03 | 98.33 |
| C1 | 41-60 | 13.57 | 3.06 | 16.58 | 3.01 | 98.37 |
| C1 | 61-80 | 13.08 | 3.10 | 16.12 | 3.04 | 97.95 |
| C1 | 81-85 | 13.26 | 3.06 | 16.25 | 2.99 | 97.64 |
| C2 | 0-20 | 13.33 | 3.04 | 16.24 | 2.91 | 95.52 |
| C2 | 21-40 | 13.43 | 3.14 | 16.31 | 2.88 | 91.55 |
| C2 | 41-60 | 13.08 | 3.16 | 16.16 | 3.08 | 97.45 |
| C2 | 61-70 | 13.50 | 3.12 | 16.58 | 3.07 | 98.48 |
| C3 | 0-20 | 13.51 | 3.18 | 16.54 | 3.03 | 95.29 |
| C3 | 21-40 | 13.23 | 3.17 | 16.31 | 3.09 | 97.36 |
| C3 | 41-60 | 12.84 | 3.16 | 15.75 | 2.91 | 92.22 |
| C3 | 61-80 | 14.12 | 3.09 | 17.14 | 3.02 | 97.65 |
| C3 | 81-85 | 13.07 | 3.05 | 16.07 | 2.99 | 98.29 |
| C4 | 0-20 | 13.36 | 3.11 | 16.40 | 3.04 | 97.90 |
| C4 | 21-40 | 13.38 | 3.15 | 16.46 | 3.08 | 97.67 |
| C4 | 41-60 | 13.08 | 3.13 | 16.04 | 2.95 | 94.21 |
| C4 | 61-77 | 13.54 | 3.11 | 16.59 | 3.05 | 98.15 |
| Sinú River-1 | 0-100 | 13.02 | 3.10 | 16.11 | 3.08 | 99.54 |
| Sinú River-2 | 0-100 | 13.56 | 3.11 | 16.65 | 3.08 | 99.12 |
| Sinú River-3 | 0-100 | 13.51 | 3.13 | 16.62 | 3.11 | 99.43 |
| SandNispeyal-1 | 0-100 | 13.39 | 3.04 | 16.43 | 3.03 | 99.77 |
| SandNispeyal-2 | 0-100 | 13.44 | 3.13 | 16.56 | 3.12 | 99.62 |
| SandNispeyal-3 | 0-100 | 13.07 | 3.05 | 16.11 | 3.04 | 99.77 |

# E - Contents Of Carbon And Nitrogen

| 1 | 2 | 3 | 4 | 5 | 6 | 7 | 8 | 9 | 10 | 11 |
|---|---|---|---|---|---|---|---|---|---|---|
| Plot Number | Depth [cm] | Weight [mg] | $C_{total}$ [%] | $N_{total}$ [%] | $C_{inorg}$ [%] | $C_{org}$ [%] | DM [mg] | $C_{total}$Corr. [%] | $N_{total}$Corr. [%] | $C_{org}$Corr. [%] |
| P21 | 0-20 | 23.45 | 31.45 | 1.28 | 0 | 31.45 | 21.92 | 33.63 | 1.37 | 33.63 |
| P21 | 21-40 | 23.34 | 28.66 | 1.02 | 0 | 28.66 | 21.78 | 30.72 | 1.09 | 30.72 |
| P21 | 41-60 | 21.29 | 27.36 | 0.86 | 0 | 27.36 | 19.77 | 29.46 | 0.93 | 29.46 |
| P21 | 61-80 | 22.85 | 27.33 | 0.75 | 0 | 27.33 | 21.61 | 28.90 | 0.80 | 28.90 |
| R1 | 0-15 | 23.02 | 28.74 | 1.32 | 0 | 28.74 | 21.60 | 30.62 | 1.41 | 30.62 |
| R1 | 16-25 | 20.74 | 23.99 | 0.96 | 0 | 23.99 | 19.69 | 25.27 | 1.01 | 25.27 |
| R1 | 26-35 | 254.48 | 10.34 | 0.40 | 0.04 | 10.31 | 246.25 | 10.69 | 0.41 | 10.65 |
| R1 | 36-57 | 257.25 | 2.07 | 0.16 | u. r. | 2.07 | 248.81 | 2.14 | 0.16 | 2.14 |
| R1-Replication | 0-15 | 23.11 | 28.42 | 1.27 | 0 | 28.42 | 21.71 | 30.25 | 1.35 | 30.25 |
| R1-Replication | 16-30 | 22.25 | 20.08 | 0.77 | 0 | 20.08 | 21.16 | 21.12 | 0.81 | 21.12 |
| R1-Replication | 31-40 | 252.46 | 8.31 | 0.35 | 0.03 | 8.28 | 244.92 | 8.57 | 0.36 | 8.54 |
| R1-Replication | 41-57 | 257.47 | 2.37 | 0.16 | u. r. | 2.37 | 252.73 | 2.41 | 0.16 | 2.41 |
| R4 | 0-20 | 22.18 | 29.61 | 1.45 | 0 | 29.61 | 20.76 | 31.64 | 1.55 | 31.64 |
| R4 | 21-40 | 20.21 | 31.00 | 1.42 | 0 | 31.00 | 18.78 | 33.35 | 1.52 | 33.35 |
| R5 | 0-20 | 22.37 | 29.46 | 1.60 | 0 | 29.46 | 20.83 | 31.64 | 1.72 | 31.64 |
| R5 | 21-40 | 22.76 | 24.41 | 1.23 | 0 | 24.41 | 21.22 | 26.19 | 1.32 | 26.19 |
| R5 | 41-50 | 252.90 | 16.55 | 0.66 | 0.03 | 16.52 | 241.00 | 17.37 | 0.69 | 17.34 |
| R5 | 51-60 | 23.44 | 26.48 | 1.11 | 0 | 26.48 | 21.97 | 28.26 | 1.18 | 28.26 |
| R5 | 61-80 | 21.46 | 24.23 | 1.15 | 0 | 24.23 | 17.52 | 29.68 | 1.41 | 29.68 |
| R5 | 81-90 | 258.69 | 15.94 | 0.63 | 0.03 | 15.91 | 246.09 | 16.76 | 0.66 | 16.73 |
| R6 | 0-20 | 23.14 | 31.43 | 1.43 | 0 | 31.43 | 21.51 | 33.82 | 1.54 | 33.82 |
| R6 | 21-27 | 20.88 | 28.17 | 1.25 | 0 | 28.17 | 19.64 | 29.95 | 1.33 | 29.95 |
| R6 | 28-45 | 20.78 | 23.94 | 0.99 | 0 | 23.94 | 19.62 | 25.36 | 1.05 | 25.36 |
| R6-Replication | 0-20 | 22.69 | 31.71 | 1.34 | 0 | 31.71 | 21.34 | 33.72 | 1.43 | 33.72 |
| R6-Replication | 21-40 | 22.54 | 25.07 | 1.16 | 0 | 25.07 | 21.25 | 26.59 | 1.23 | 26.59 |
| R6-Replication | 41-47 | 20.10 | 17.37 | 0.73 | 0 | 17.37 | 19.23 | 18.15 | 0.77 | 18.15 |
| R6-Replication | 48-54 | 257.23 | 14.49 | 0.57 | u. r. | 14.49 | 247.60 | 15.05 | 0.60 | 15.05 |
| P16 | 0-20 | 20.55 | 23.66 | 1.53 | 0 | 23.66 | 19.48 | 24.97 | 1.61 | 24.97 |
| P16 | 21-30 | 20.17 | 18.90 | 1.07 | 0 | 18.90 | 19.15 | 19.91 | 1.13 | 19.91 |
| P16 | 31-50 | 255.66 | 3.22 | 0.23 | u. r. | 3.22 | 235.21 | 3.50 | 0.25 | 3.50 |
| P16 | 51-65 | 253.37 | 3.19 | 0.20 | u. r. | 3.19 | 248.61 | 3.25 | 0.21 | 3.25 |
| P16 | 66-85 | 259.06 | 3.11 | 0.23 | u. r. | 3.11 | 235.20 | 3.43 | 0.25 | 3.43 |
| P16 | 86-95 | 253.28 | 1.75 | 0.14 | u. r. | 1.75 | 249.78 | 1.77 | 0.14 | 1.77 |
| C1 | 0-20 | 257.62 | 2.94 | 0.22 | u. r. | 2.94 | 252.28 | 3.00 | 0.23 | 3.00 |
| C1 | 21-40 | 256.08 | 1.45 | 0.14 | u. r. | 1.45 | 251.80 | 1.47 | 0.15 | 1.47 |
| C1 | 41-60 | 254.43 | 1.31 | 0.14 | u. r. | 1.31 | 250.29 | 1.33 | 0.14 | 1.33 |
| C1 | 61-80 | 251.55 | 1.85 | 0.16 | u. r. | 1.85 | 246.38 | 1.89 | 0.16 | 1.89 |
| C1 | 81-85 | 259.53 | 6.07 | 0.38 | u. r. | 6.07 | 253.41 | 6.21 | 0.39 | 6.21 |
| C2 | 0-20 | 252.89 | 17.74 | 0.95 | 0.04 | 17.70 | 241.55 | 18.58 | 1.00 | 18.54 |
| C2 | 21-40 | 257.38 | 4.76 | 0.33 | u. r. | 4.76 | 235.64 | 5.19 | 0.36 | 5.19 |
| C2 | 41-60 | 258.04 | 3.73 | 0.27 | u. r. | 3.73 | 251.46 | 3.83 | 0.27 | 3.83 |
| C2 | 61-70 | 250.32 | 2.62 | 0.16 | u. r. | 2.62 | 246.52 | 2.66 | 0.16 | 2.66 |
| C3 | 0-20 | 20.96 | 20.85 | 1.06 | 0 | 20.85 | 19.97 | 21.88 | 1.11 | 21.88 |
| C3 | 21-40 | 259.46 | 10.80 | 0.54 | 0.03 | 10.76 | 252.62 | 11.09 | 0.56 | 11.06 |
| C3 | 41-60 | 258.76 | 5.66 | 0.38 | 0.03 | 5.63 | 238.62 | 6.14 | 0.41 | 6.11 |
| C3 | 61-80 | 255.13 | 5.04 | 0.33 | 0.03 | 5.01 | 249.13 | 5.16 | 0.34 | 5.13 |
| C3 | 81-85 | 254.35 | 4.44 | 0.30 | 0.03 | 4.40 | 249.99 | 4.51 | 0.31 | 4.48 |
| C4 | 0-20 | 254.60 | 4.71 | 0.40 | 0.03 | 4.67 | 249.25 | 4.81 | 0.40 | 4.78 |
| C4 | 21-40 | 258.89 | 1.53 | 0.16 | u. r. | 1.53 | 252.85 | 1.57 | 0.17 | 1.57 |
| C4 | 41-60 | 251.58 | 1.50 | 0.16 | u. r. | 1.50 | 237.02 | 1.60 | 0.17 | 1.60 |
| C4 | 61-77 | 255.16 | 1.67 | 0.16 | u. r. | 1.67 | 250.45 | 1.71 | 0.16 | 1.71 |
| Sinú River-1 | 0-100 | 502.28 | 0.33 | 0.04 | 0.04 | 0.29 | 499.98 | 0.33 | 0.04 | 0.29 |
| Sinú River-2 | 0-100 | 500.53 | 0.77 | 0.09 | 0.02 | 0.75 | 496.12 | 0.77 | 0.09 | 0.75 |
| Sinú River-3 | 0-100 | 507.66 | 0.58 | 0.07 | 0.02 | 0.56 | 504.77 | 0.59 | 0.07 | 0.57 |
| SandNispeyal-1 | 0-100 | 60.97 | 11.09 | 0.04 | 10.33 | 0.77 | 60.83 | 11.12 | 0.04 | 0.79 |
| SandNispeyal-2 | 0-100 | 65.12 | 11.50 | 0.06 | 10.37 | 1.13 | 64.87 | 11.55 | 0.06 | 1.17 |
| SandNispeyal-3 | 0-100 | 66.23 | 11.40 | u. r. | 10.82 | 0.58 | 66.08 | 11.43 | 0.00 | 0.61 |
| $CaCO_3$ | Standard | 60.75 | 11.97 |  | 11.89 | 0.08 |  |  |  |  |

# F - Results Of Isotope, Al- And Fe- Oxide Measurements

| Plot Number | Depth [cm] | $\delta^{13}C$ [‰] | $F^{14}C$ | err | $\Delta^{14}C$ [‰] | err [‰] | $Al_o$ [mg/L] | $Fe_o$ [mg/L] | $Al_d$ [mg/L] | $Fe_d$ [mg/L] |
|---|---|---|---|---|---|---|---|---|---|---|
| P21 | 0-20 | -28,38 | 1,15 | 0,0027 | 140,20 | 2,70 | 5.03 | 5.87 | 0,00 | 0.078 |
| P21 | 21-40 | -28,29 | 1,23 | 0,00 | 220,10 | 2,60 | | | | |
| P21 | 41-60 | -28,41 | 1,03 | 0,00 | 22,60 | 2,40 | 12.4 | 26.3 | 0.223 | 0.767 |
| P21 | 61-80 | -28,87 | 1,00 | 0,00 | -12,40 | 2,40 | 15.4 | 42.5 | 0.069 | 0.871 |
| R1 | 0-15 | -28,24 | | | | | | | | |
| R1 | 16-25 | -28,75 | | | | | | | | |
| R1 | 26-35 | -28,68 | | | | | | | | |
| R1 | 36-57 | -28,26 | | | | | | | | |
| R1-Replication | 0-15 | -27,96 | | | | | 6.12 | 9.16 | 0,00 | 0.134 |
| R1-Replication | 16-30 | -28,57 | | | | | 14.2 | 25.3 | 0.029 | 0.501 |
| R1-Replication | 31-40 | -28,53 | | | | | 16.1 | 37.5 | 0.087 | 1.09 |
| R1-Replication | 41-57 | -28,21 | | | | | 16.1 | 44.3 | 0.279 | 2.29 |
| R4 | 0-20 | -28,86 | | | | | 3.24 | 5.86 | 0,00 | 0.067 |
| R4 | 21-40 | -28,64 | | | | | 0.895 | 2.43 | 0,00 | 0,00 |
| R5 | 0-20 | -28,78 | 1,12 | 0,01 | 108,70 | 5,50 | 3.98 | 8.9 | 0,00 | 0.154 |
| R5 | 21-40 | -28,43 | 1,31 | 0,00 | 301,90 | 3,10 | 12.1 | 12.5 | 0.032 | 0.234 |
| R5 | 41-50 | -28,44 | 1,01 | 0,00 | 5,40 | 2,40 | 14.8 | 25.7 | 0.09 | 0.553 |
| R5 | 51-60 | -29,13 | 1,09 | 0,00 | 82,00 | 2,60 | | | 0,00 | 0.395 |
| R5 | 61-80 | -28,82 | 1,14 | 0,00 | 131,90 | 2,80 | 6.88 | 24.7 | 0,00 | 0.537 |
| R5 | 81-90 | -28,55 | 1,00 | 0,00 | -12,00 | 2,20 | 13.9 | 18 | 0.08 | 0.506 |
| R6 | 0-20 | -29,15 | | | | | | | | |
| R6 | 21-27 | -28,76 | | | | | | | | |
| R6 | 28-45 | -29,10 | | | | | | | | |
| R6-Replication | 0-20 | -28,98 | | | | | 3.21 | 2.93 | 0,00 | 0.05 |
| R6-Replication | 21-40 | -29,06 | | | | | 9.4 | 15.7 | 0.023 | 0.395 |
| R6-Replication | 41-47 | -28,31 | | | | | 15 | 16.1 | 0.135 | 0.399 |
| R6-Replication | 48-54 | -28,65 | | | | | 12.1 | 30.4 | 0.134 | 1.06 |
| P16 | 0-20 | -26,91 | 1,12 | 0,00 | 112,20 | 4,90 | 9.79 | 11.8 | 0.065 | 0.348 |
| P16 | 21-30 | -27,44 | 1,24 | 0,01 | 232,90 | 6,20 | 11.3 | 19.4 | | |
| P16 | 31-50 | -28,97 | 0,98 | 0,00 | -31,70 | 4,70 | 13.9 | 57.5 | 0.526 | 2.17 |
| P16 | 51-65 | -28,56 | 0,90 | 0,01 | -102,60 | 5,10 | 15 | 84.7 | 0.205 | 2.14 |
| P16 | 66-85 | -28,71 | 0,94 | 0,01 | -63,70 | 5,10 | 15.9 | 74.9 | 0.402 | 1.96 |
| P16 | 86-95 | -28,45 | 0,85 | 0,01 | -154,70 | 5,60 | 16.4 | 103 | 0.286 | 2.88 |
| C1 | 0-20 | -27,18 | | | | | 12.6 | 103 | 0.294 | 4.39 |
| C1 | 21-40 | -24,66 | | | | | 13.2 | 131 | 0.259 | 5.5 |
| C1 | 41-60 | -25,52 | | | | | 14 | 127 | 0.318 | 4.7 |
| C1 | 61-80 | -27,46 | | | | | 18.4 | 116 | 0.312 | 3.28 |
| C1 | 81-85 | -29,09 | | | | | 15.7 | 61.6 | 0.346 | 1.39 |
| C2 | 0-20 | -28,28 | | | | | 12.9 | 16.7 | 0.1 | 0.455 |
| C2 | 21-40 | -28,64 | | | | | 12.7 | 28 | 0.623 | 1.24 |
| C2 | 41-60 | -28,28 | | | | | 15.3 | 88.5 | 0.38 | 3.31 |
| C2 | 61-70 | -27,95 | | | | | 17.9 | 126 | 0.245 | 3.09 |
| C3 | 0-20 | -27,81 | | | | | 15.1 | 11.4 | 0.059 | 0.196 |
| C3 | 21-40 | -27,79 | | | | | 13 | 9.03 | 0.133 | 0.178 |
| C3 | 41-60 | -26,80 | | | | | 16.7 | 69 | 0.599 | 2.28 |
| C3 | 61-80 | -27,24 | | | | | 15.5 | 62.6 | 0.198 | 1.53 |
| C3 | 81-85 | -27,26 | | | | | 15 | 59.6 | 0.226 | 1.3 |
| C4 | 0-20 | -27,54 | | | | | 13.3 | 101 | 0.275 | 3.53 |
| C4 | 21-40 | -25,36 | | | | | 13.7 | 129 | 0.197 | 3.73 |
| C4 | 41-60 | -26,34 | | | | | 16 | 93.5 | 0.53 | 6.16 |
| C4 | 61-77 | -27,56 | | | | | 14.4 | 103 | 0.701 | 4.58 |
| C4 | 0-10 | | 1,03 | 0,00 | 25,80 | 2,90 | | | | |
| C4 | 10-20 | | 0,86 | 0,00 | -147,20 | 2,40 | | | | |
| C4 | 20-30 | | 0,73 | 0,00 | -277,30 | 2,10 | | | | |
| C4 | 30-36 | | 0,68 | 0,00 | -329,90 | 1,90 | | | | |
| C4 | 37-47 | | 0,66 | 0,00 | -343,30 | 2,20 | | | | |
| C4 | 47-57 | | 0,62 | 0,00 | -382,00 | 1,90 | | | | |
| C4 | 57-64 | | 0,72 | 0,00 | -287,00 | 2,30 | | | | |
| C4 | 64-74 | | 0,79 | 0,00 | -220,90 | 2,50 | | | | |
| C4 | 74-84 | | 0,80 | 0,00 | -209,00 | 2,10 | | | | |
| Sinú River-1 | 0-100 | -26,01 | 0,59 | 0,00 | -419,60 | 4,40 | 14 | 82.4 | 0.241 | 2.41 |
| Sinú River-2 | 0-100 | -26,91 | 0,77 | 0,00 | -236,10 | 4,40 | 12.2 | 103 | 0.45 | 4.38 |
| Sinú River-3 | 0-100 | -27,33 | 0,76 | 0,00 | -250,30 | 4,20 | | | | |
| SandNispeyal-1 | 0-100 | -3,31 | | | | | 1.55 | 5.98 | 0,00 | 0.142 |
| SandNispeyal-2 | 0-100 | -4,15 | | | | | 2.13 | 6.83 | 0,00 | 0.157 |
| SandNispeyal-3 | 0-100 | -2,43 | 0,79 | 0,01 | -214,1 | 10,0 | | | | |

# G - XRD Patterns Of Special Clay Mineral Treatment

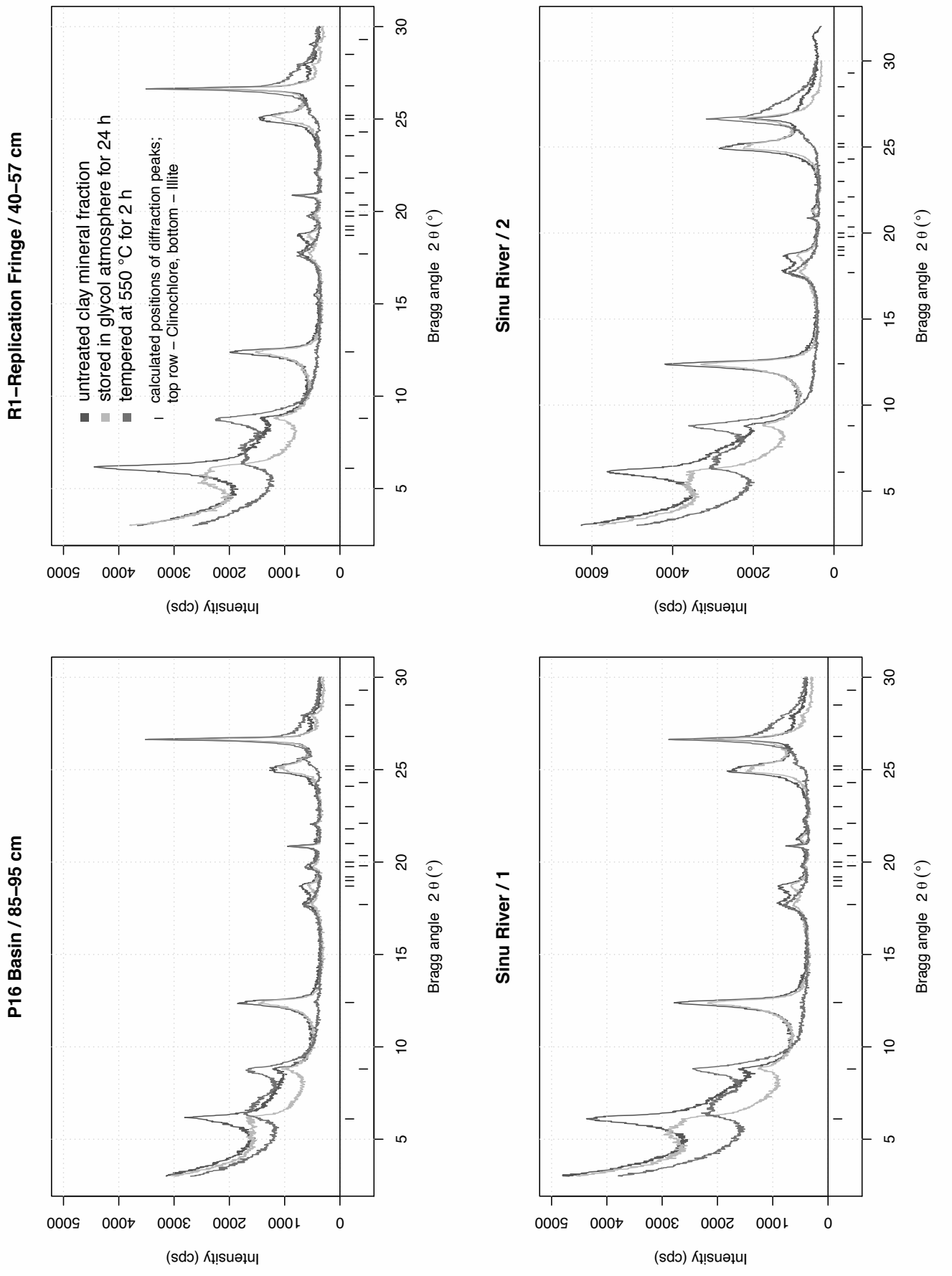

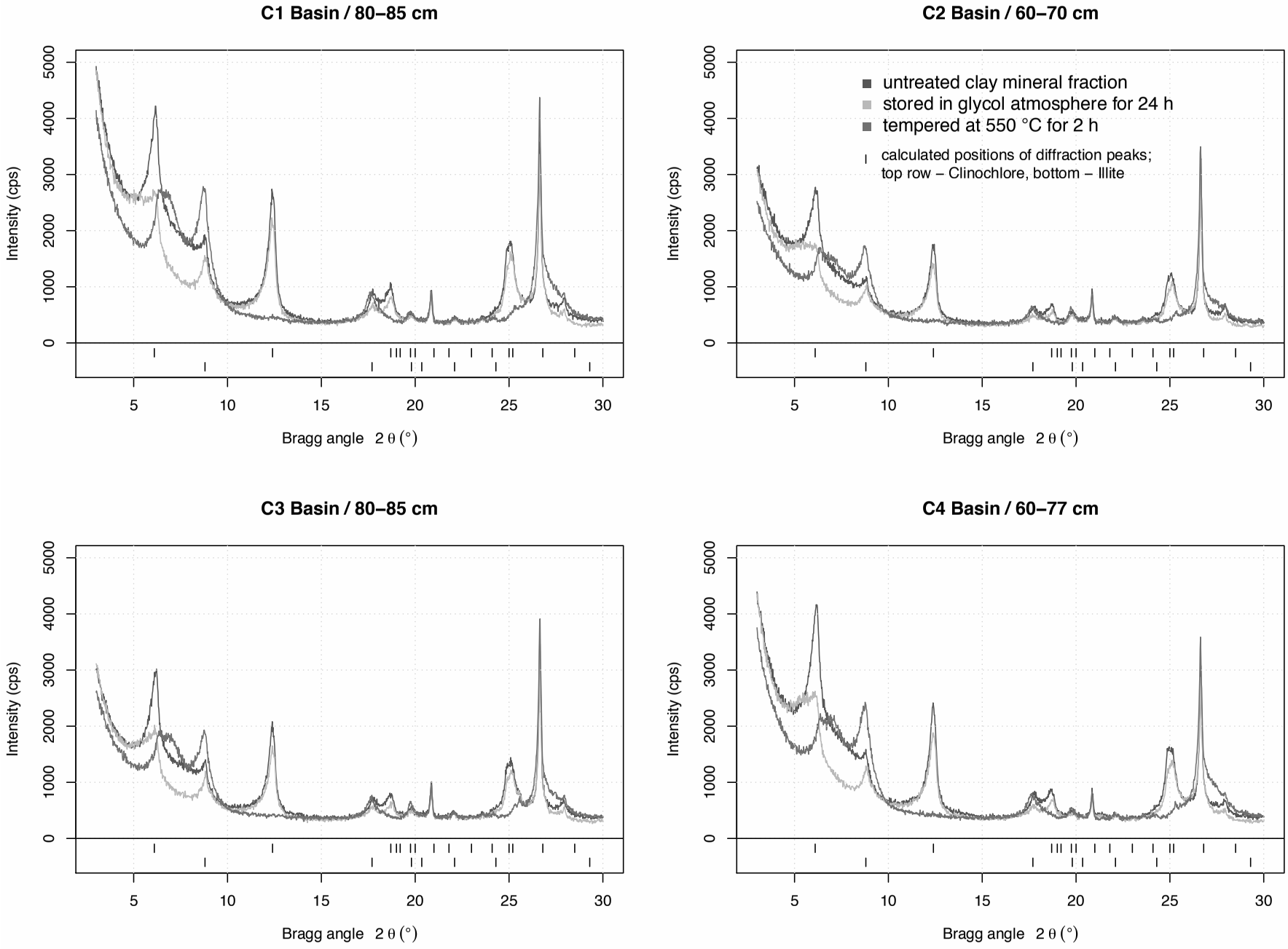
C1 Basin / 80–85 cm
C2 Basin / 60–70 cm
C3 Basin / 80–85 cm
C4 Basin / 60–77 cm
Intensity (cps)
Bragg angle 2 θ (°)
untreated clay mineral fraction
stored in glycol atmosphere for 24 h
tempered at 550 °C for 2 h
calculated positions of diffraction peaks;
top row – Clinochlore, bottom – Illite